

The Observed Impact of the Lower Stratospheric Thermodynamic Environment on Overshooting Top Characteristics during the RELAMPAGO-CACTI Field Campaign

Melinda T. Berman¹, Robert J. Trapp¹, Stephen W. Nesbitt¹ and Larry Di
Girolamo¹

¹Department of Climate, Meteorology and Atmospheric Sciences, University of Illinois
Urbana-Champaign, Urbana, IL 61801

Key Points:

- OTs with the largest area occur across the study domain while OTs with the largest depth occur largely in one cluster
- Overshooting top area is weakly related to LS static stability
- Overshooting top depth is weakly to moderately related to LS static stability

Abstract

Overshooting tops (OTs) are manifestations of deep convective updrafts that extend above the tropopause into the stratosphere. They can induce dynamic perturbations and result in irreversible transport of aerosols, water vapor and other mass from the troposphere into the stratosphere, thereby impacting the chemical composition and radiative processes of the stratosphere. These and other effects of OTs depend on their characteristics such as depth and area, which are understood to connect to mid-tropospheric updraft speed and width, respectively. Less understood is how static stability in the lower stratosphere (LS) potentially modulates these OT–updraft connections, thus motivating the current study. Here, LS static stability and observed OT characteristics are quantified and compared using a combination of reanalysis data, observed rawinsonde data and geostationary satellite data. A weak to moderate relationship between OT depth and LS lapse rate and Brunt-Väisälä frequency (N^2) ($R = 0.38, -0.37$, respectively) is found, implying that OT depth is reduced with an increasingly stable LS. In contrast, a weak relationship ($R = -0.03, 0.03$, respectively) is found between OT area and LS static stability, implying that OT area is controlled primarily by mid to upper tropospheric updraft area. OT duration has a weak relationship to LS lapse rate and N^2 ($R = 0.02, -0.02$, respectively). These relationships may be useful in interpreting mid- and low-level storm dynamics from satellite-observed characteristics of OTs in near real-time.

Plain Language Summary

An overshooting top (OT) is a domed protrusion of a storm that reaches the stratosphere. These phenomena are important for their impact on stratospheric chemistry and their relationship to on-the-ground severe weather hazards. Spatial trends in OTs in southeastern South America are explored. Additionally, it is shown that static stability in the LS can be related to some aspects of OTs.

1 Introduction

Overshooting tops (OTs) are manifestations of deep convective updrafts that extend above the tropopause into the stratosphere. They can result in irreversible transport of aerosols to the stratosphere and induce dynamic perturbations in the upper troposphere and lower stratosphere (UTLS) (Bernath et al., 2022; Fromm et al., 2010; Holton et al., 1995; Pan et al., 2014). OTs can also induce intense gravity waves and hydraulic jumps, leading to additional turbulent mixing in the lowermost stratosphere (Lane et al., 2003; O’Neill et al., 2021; Wang, 2003). The cross-tropopause transport (CTT) induced by OTs can impact stratospheric chemistry (Dauhut et al., 2018; Fischer et al., 2003; Fueglistaler et al., 2009). For example, CTT has been shown to mix stratospheric ozone to the troposphere which has important climate impacts, many of which are currently not well represented in global climate models (Huntrieser et al., 2016; Schroeder et al., 2014; S. Solomon et al., 2010; Pan et al., 2014). CTT is sensitive to static stability, which is high in the tropopause layer and can limit the amount of transport from tropospheric buoyancy alone (Birner, 2006; Gordon & Homeyer, 2022). An additional forcing mechanism, such as a particularly strong and deep, tropospheric convective updraft may be necessary to overcome this high static stability.

CTT can also lead to stratospheric moistening, as OTs can inject water vapor into the stratosphere (Dauhut et al., 2018; Hegglin et al., 2004; Khordakova et al., 2022; Setvák et al., 2008). Field observations have shown that OTs can noticeably moisten the stratosphere due to frozen condensate transport (Herman et al., 2017). Idealized modeling has also indicated that the height of the OT can play a role in the amount of entrainment and moistening that occurs (Dauhut et al., 2018). Water vapor in the stratosphere can also impact radiative heating rates and modify surface warming due to its impact on in-

coming and outgoing radiation, another climate implication of OTs (S. Solomon et al., 2010).

Specific characteristics of OTs are understood to be related to tropospheric updraft characteristics. Horizontal OT area (OTA) has been shown to strongly positively correlate to updraft area (Trapp et al., 2017), and it is assumed the vertical depth of OTs (OTD) is related to updraft speed (Fujita, 1974; Heymsfield et al., 2010). Moreover, OTs and above-anvil cirrus plumes often indicate the occurrence of ground-based hazardous weather including tornadoes, severe winds, hail and flooding (Adler & Fenn, 1979; Bedka et al., 2018; Dworak et al., 2012; Homeyer et al., 2017; Marion et al., 2019). Thus, a link exists between observed storm-top characteristics, mid to upper tropospheric updrafts and the ground-level hazards that most directly impact people.

An understudied complication to this link is the local thermodynamic environment in the LS. Fujita (1974) presents a theoretical framework for this complication by hypothesizing the impact of lapse rates in the LS, from the equilibrium level to the top of the OT on OTD. Based on parcel theory, the hypothesized relationship between the maximum height of the overshooting top (∂z_m), the updraft speed at the crossover point (w_m), the environmental temperature at the equilibrium level (T) and the difference in the lapse rates inside and outside the cloud, (Γ' and Γ), respectively, is given as:

$$\partial z_m = w_m \sqrt{\frac{T}{g(\Gamma' - \Gamma)}} \quad (1)$$

Fujita's framework, however, does not provide guidance on how LS thermodynamics might impact OTA, nor does it address non-linear processes.

More recently, Homeyer et al. (2014a, 2014b), D. L. Solomon et al. (2016) and Gordon and Homeyer (2022) provide insight into how LS stability may impact cross-tropopause transport by OTs and OTD. These studies, however, take a simplified view of static stability at the tropopause by largely examining only differences in tropopause configurations, such as single versus double tropopause structures. More analysis is needed to examine a wider range of both observed characteristics of overshooting tops as well as measures of static stability beyond tropopause configuration.

Our study extends these previous efforts and examines how LS static stability affects OTA, OTD and OT duration (OTT), for a large population of observed OTs. For identical updraft cores, a more stable LS may modify OTA, OTD and OTT differently than would a less stable LS. Understanding the relationships between OT characteristics and mid- and lower-level tropospheric updraft characteristics will improve our interpretation of the physical relationship between OTs and near-surface hazardous weather, and provide insight into transport mechanisms between the troposphere and the stratosphere. This understanding could improve the representation of convective processes in weather and climate models.

2 Data

2.1 Study Domain

OTs were analyzed over southeastern South America (SESA), which is known to have some of the deepest convective storms on Earth (Liu et al., 2020; Zipser et al., 2006). The Remote Sensing of Electrification, Lightning, and Mesoscale/Microscale Processes with Adaptive Ground Observations- Clouds, Aerosols, and Complex Terrain Interactions (RELAMPAGO-CACTI) field campaign took place in SESA, with most observations taken from 1 November 2018 - 31 January 2019 (Nesbitt et al., 2021; Varble et al., 2021). IOPs included regular launching of radiosondes during RELAMPAGO (Nesbitt et al., 2021) and enhanced frequencies of regularly launched CACTI radiosondes (Varble

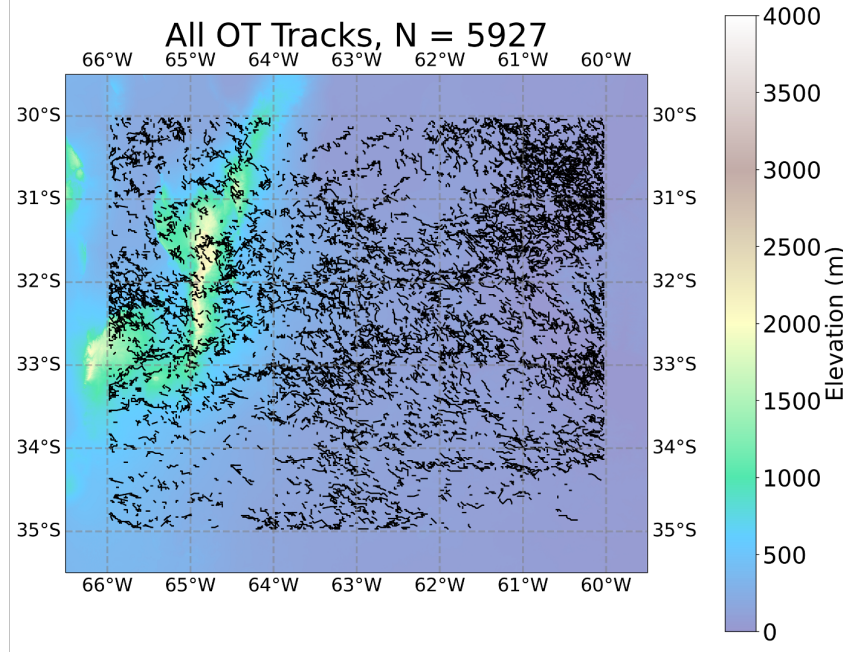


Figure 1. Topographical map of SESA showing the study domain and all 5928 analyzed OT tracks.

et al., 2021). Figure 1 shows the study domain, a subsection of the larger RELAMPAGO domain (see Figure 6; Nesbitt et al. (2021)), ranging from 30° to 35° S and 66° to 60° W. Also shown in Figure 1 is the topography of the region, highlighting the Sierras de Córdoba mountain range and the tracks (defined below) of all the analyzed OTs during the study period, November 2018-February 2019. Tracks within 0.02° of the boundary were removed to lessen the impact of artificial shortening of track length and duration by tracks that intersect the boundary.

2.2 Observational Data

RELAMPAGO-CACTI radiosonde data were used to validate the reanalysis-derived atmospheric profiles discussed in Section 3. Radiosondes were routinely launched from a variety of fixed (entire campaign) and mobile (IOPs only) locations during RELAMPAGO-CACTI.

One-minute Mesoscale Domain Sector (MDS) data from the Geostationary Operational Environmental Satellite (GOES)-16 (GOES-East during the study period) were used to identify the OTs in the SESA study domain. A detailed description of the OT detection method can be found in Khlopenkov et al. (2021). Generally, OTs were detected using visible reflectance imagery (Band 2), longwave infrared brightness temperature imagery (Band 13) (Schmit et al., 2017) and a blended reanalysis tropopause, with detection probabilities based on the tropopause-normalized temperature, the prominence of the OT, the anvil area and the uniformity of the temperature of the anvil (Khlopenkov et al., 2021). Note that because MDS scans were requested intermittently during the field campaign during selected convective events, there is not a continuous record of these high-resolution data for the entire study period.

2.3 MERRA-2 Reanalysis Data

The Modern-Era Retrospective analysis for Research and Applications, Version 2 (MERRA-2) was used to quantify the environment and the static stability parameters in the LS (Gelaro et al., 2017). MERRA-2 has been used widely in studies examining the LS and its associated characteristics (Cooney et al., 2021; Khlopenkov et al., 2021; Schmit et al., 2017; Wargan & Coy, 2016). All widely used reanalysis products (MERRA-2, ERA-Interim, JSA-55, CSFR) perform similarly with relatively small biases in the LS region, relative to the resolution of the models (Xian & Homeyer, 2019). Several datasets from MERRA-2 were used to derive the thermodynamic and tropopause characteristics, namely the 3-hourly, model level, assimilated (M2I3NVASM) and the 1-hourly, instantaneous, single-level, assimilated (M2I1NXASM) datasets. The details for the treatment of the data are described in Section 3.

3 Methodology

3.1 Statistical Methods

Relationships between the OT characteristics and static stability were examined in two ways. First, the mean values of OTA and OTD for each track were analyzed as 2D histograms, as were the duration and length of each OT track. The Pearson correlation coefficient, (R) and p-value using the Wald test (P) using the SciPy linear regression function were calculated from the, when applicable, track-mean values (Virtanen et al., 2020). The p-value indicates whether the null hypothesis that the regression line has zero slope can be rejected at some level. All p-values with magnitudes less than $1 * 10^{-10}$ are reported as 0 in the relevant figures with the actual values reported in the text. Then, the mean values of OTA and OTD per track, OTT or track length were binned into 10 bins. Because there is a high concentration of data around a relatively small range of values, the binning highlights the full distribution of the data. Figure 2 shows an example of this process. The 2D histogram shows the distribution of the length and duration for each track. The violin plots overlaid on the histogram show the distribution of the data in each of the 10 bins as well as the medians and extrema for each violin.

3.2 Identification of OT Characteristics and OT Tracking

In this study, all OTs with a detection probability greater than 0.8, as determined by the Khlopenkov et al. (2021) method, were analyzed. This threshold ensures high enough confidence in detections without removing too many OT candidate objects (Bedka & Khlopenkov, 2016; Grover, 2021) to balance OT detection while minimizing the false alarm ratio. Cooney et al. (2021) compares varying OT probability thresholds to radar derived OTs and finds a probability greater than 0.5 is generally suitable for OTs. While 0.8 may lower the probability of detection for OTs (Cooney et al., 2021), it minimizes the false alarm ratio as well. OTs were removed because they had negative OT depths (i.e., they fell below the MERRA-2 tropopause) (316 OTs), there were not enough height levels for corresponding static stability calculations (83 OTs) or their calculated area was less than 4 km^2 (808 OTs). At least three pressure levels were needed to get the average static stability values for the interpolation layer. Once all OTs in a satellite scene were identified, Scikit-image was used to label and cluster OTs that were neighbors in at least a 2-connected sense (van der Walt et al., 2014); this ensured that connected areas of low brightness temperature were not considered separate OTs. The center of these clusters was then used to identify the relevant OT characteristics for analysis.

OTs were tracked using the trackpy Python package (v0.6.1, (Allen et al., 2023)). Trackpy is an image processing package that links related features and is based on Crocker and Grier (1996). Identified features were linked together using a 5700-m search range defined by the maximum velocity (here 95 m s^{-1} , towards the maximum potential value

of LS winds) and the 1-minute time frequency of the data. The memory of the algorithm, or how long a feature can be absent and still be included in the track, was 2 minutes. This was determined by testing different thresholds for the memory. Of the 31,936 OTs detected, 31,127 OTs were analyzed and 5927 tracks were formed. 2643 OTs were removed from the tracked analysis because they are stubs, or OTs where the track length is shorter than the memory chosen.

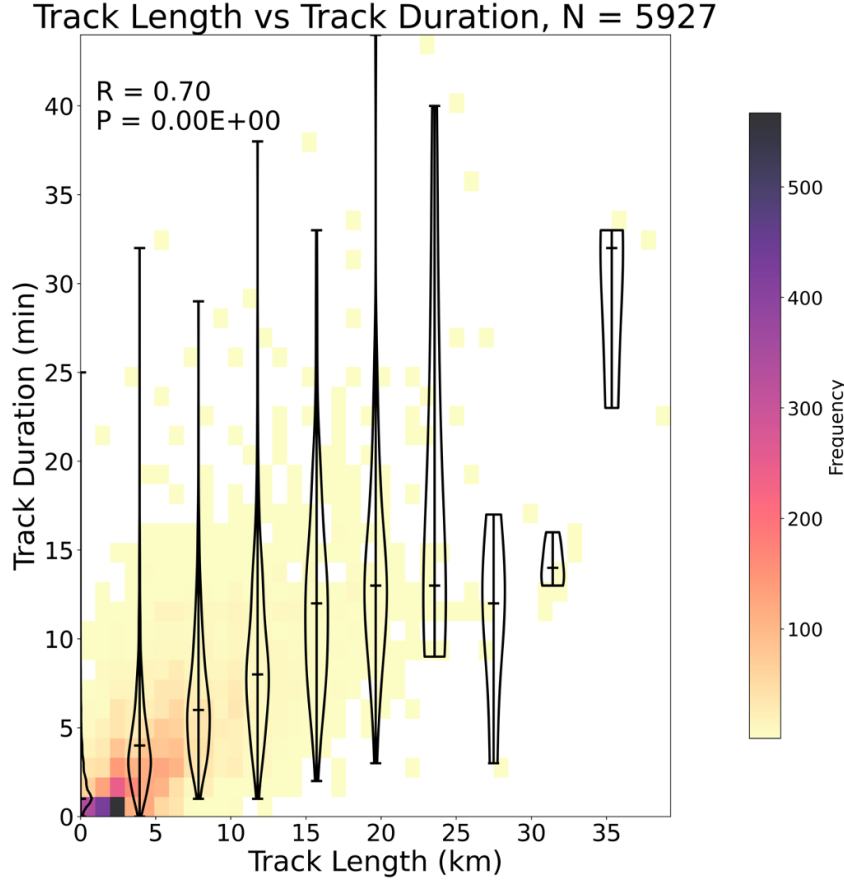


Figure 2. 2D Histogram of track length vs track duration for all OT tracks. Also shown are violin plots for the binned data with the median line. The R and P values correspond to the raw data in the 2D histogram.

OTT was calculated by summing the total tracked time of each OT. The first time an OT appears is the beginning time for the track. The ending time of the track is when the OT track ends for more than 2 minutes, the memory of the algorithm. If the OT reappears within 2 minutes, the track and OTT continue. OTT was calculated using the UTC beginning and ending times, rather than the number of time steps associated with the track. Figure 2 shows the relationship between track length and duration for each track. A highly linear relationship between duration and length ($R = 0.70$, $P = 0$), shows that longer OT tracks tend to correspond to longer lived OTs. This relationship is supported by the binned data as well, the median track length of the binned data generally increases with increasing track duration.

OTA was calculated using the method developed by Marion et al. (2019) and then modified by Grover (2021). With this method, brightness temperature (T_b) was evaluated along radials outward from the center of the OT, defined by the minimum bright-

ness temperature (T_{OT}), until an inflection point was reached, i.e., $\frac{d^2 T_b}{dr^2} \leq 0$. These radials from the center of the OT to the inflection points thus form the OT edges. If one radial was two standard deviations longer than the other radials, it was replaced with a radial that is equal to the average distance of the other radials. The OT polygon was projected onto the Earth and the polygon's area was calculated. OTs with an area less than 4 km^2 were removed as they are smaller than GOES resolution. Figure 3a shows the IR brightness temperature data and an identified OT with the corresponding area polygon on 25 January 2019. OTA uncertainty calculations follow the method in Di Girolamo and Davies (1997). OTA estimates have an average uncertainty of 27.38 km^2 .

Finally, OTD was calculated as:

$$OTD = \frac{T_{OT} - T_{tropopause}}{8.5} \quad (2)$$

where $T_{tropopause}$ is the tropopause temperature, calculated by converting the MERRA-2 tropopause pressure into a temperature using the environmental temperature profile from MERRA-2. $8.5 \text{ }^\circ\text{C km}^{-1}$ was chosen as the midpoint of the values from Adler et al. (1983) (8°C km^{-1}) and Negri (1982) ($9 \text{ }^\circ\text{C km}^{-1}$). Differences in the estimates of OTD using the two tropopause datasets were quantified and an average difference 0.06 km was found.

3.3 MERRA-2 Thermodynamic Profiles and Tropopause

Defining the tropopause accurately is important for characterizations of OTs. For this study, the tropopause pressure is the highest pressure (lowest altitude) between the thermal and potential vorticity tropopauses from MERRA-2, similar to the method used in Schoeberl et al. (2022). While this may induce a high bias in OTD, choosing the lower altitude tropopause is an attempt to combat the known high bias in MERRA-2 tropopause altitudes, especially prevalent in the Southern Hemisphere midlatitudes (Fujiwara et al., 2022; Xian & Homeyer, 2019). This also helps combat double tropopause profiles (Schoeberl et al., 2022).

The MERRA-2 data were horizontally smoothed using a bivariate spline interpolation and also vertically interpolated to 5 hPa intervals over the tropopause level to 50 hPa above the tropopause. The resolution of this layer was increased to 5 hPa intervals from the native MERRA-2 resolution of 72 hybrid-eta levels from the surface to 0.01 hPa (Gelaro et al., 2017). The vertical resolution of MERRA-2 in the LS is variable from 10 hPa to 50 hPa (Bosilovich et al., 2016). Figure 3b shows a reconstructed MERRA-2 sounding following this process along with the most-unstable parcel process curve and the MERRA-2-derived tropopause height. Also shown is the top of the 50 hPa analysis layer as discussed below. OTs are assigned profiles that are the nearest in space of the interpolated data and the nearest time before the OT.

3.3.1 Calculation of LS Static Stability

Once the MERRA-2 data were processed, the thermodynamic variables used to quantify static stability in the LS were calculated using the SHARPy and METpy Python packages (Blumberg et al., 2017; May et al., 2022). Lapse rate and the Brunt-Väisälä frequency squared (N^2) were quantities chosen to represent static stability in the LS, defined as the layer between the tropopause and 50 hPa above the tropopause. These parameters can be readily calculated and do not depend on the characteristics of the parcel being lifted. Entrainment and other non-adiabatic processes can cause a parcel to deviate from its parcel theory-expected behavior during moist adiabatic ascent and can be difficult to quantify. Reanalysis data also do not include potential modifications to the LS environment due to gravity waves or transport of water vapor, a limitation of this study. While testing showed that LS static stability calculations yielded similar values for both variable and fixed layers, the fixed layer is preferred. Because both lapse rate



Figure 3. IR brightness temperature map from GOES-16 with an identified OT and area polygon a) and a reconstructed MERRA-2 sounding showing the most-unstable parcel process curve (black-dashed), height of tropopause (blue) and the top of the 50 hPa analysis level (orange) b). The black arrow represents the 50 hPa analysis layer, while the blue arrow points to the parcel process curve.

and N^2 depend on layer depth, a fixed layer removes a potential confounding variable in the analysis. The depth of the layer may impact the calculations, but this can be removed by using a consistent layer to evaluate static stability.

Lapse rate, Γ ($^{\circ}\text{C km}^{-1}$), was calculated using the SHARPy lapse rate function as the change in the temperature from the bottom of the layer (Z_1 , T_1) to the top of the layer (Z_2 , T_2):

$$\Gamma = -\frac{dT}{dZ} \approx -\frac{(T_2 - T_1)}{(Z_2 - Z_1)} \quad (3)$$

Negative lapse rates are more stable layers in which temperature increases with height while small, positive lapse rates are less stable layers. Eq. (3) was calculated over each 5-hPa pressure level in the LS layer, and then averaged to estimate an LS layer-mean lapse rate. N^2 (s^{-2}) was calculated as:

$$N^2 = \frac{g}{\theta} \frac{d\theta}{dZ} = \frac{g}{T} (\Gamma_d - \Gamma) \quad (4)$$

where, g is standard gravity (m s^{-2}), θ is the potential temperature (K) and $\frac{d\theta}{dZ}$ is the change in potential temperature over the height of each 5 hPa layer. Potential temperature was calculated at each level and $\frac{d\theta}{dZ}$ was calculated using centered finite differences. Eq. (4) was also calculated over each 5 hPa pressure level in the LS layer, and then averaged to estimate an LS layer-mean N^2 .

To provide a tropospheric reference for these LS parameters, CAPE was computed using the most unstable parcel. Even though MUCAPE can overestimate the integrated buoyancy (Bunkers et al., 2002), it was chosen as opposed to a surface or mixed-layer parcel because it is applicable to elevated convection that often occurs at night, allowing for consistent CAPE calculations across all types of convection (Rochette et al., 1999; Bunkers et al., 2002).

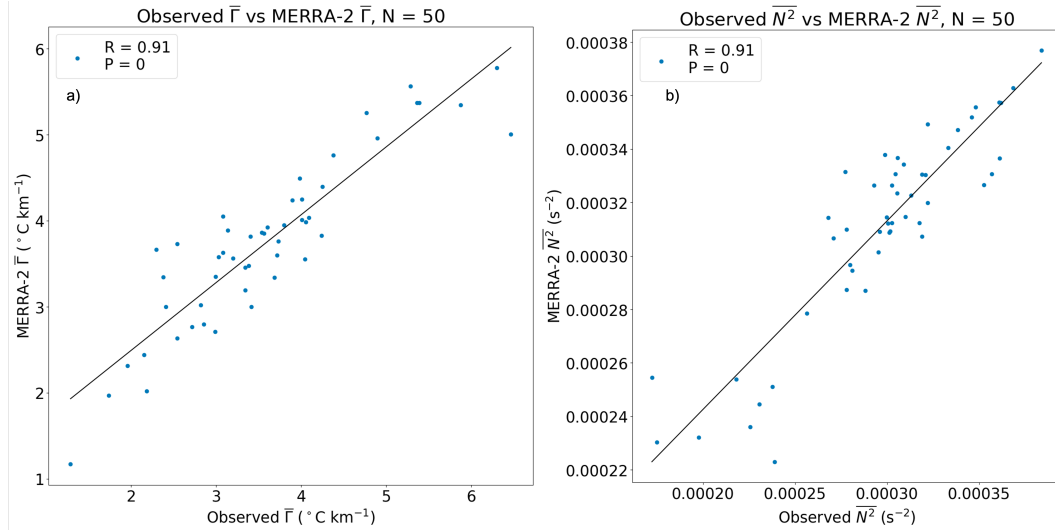


Figure 4. Comparison between the observed radiosonde and MERRA-2 values for mean lapse rate a) and mean N^2 b) for 200 hPa to 75 hPa. Also shown are the lines of best fit and R and P values.

MERRA-2 reanalysis data were compared to observed sounding data from RELAMPAGOCACCTI to determine if the reanalysis data were sufficiently representative of the observed

environments in which the OTs formed and evolved. Fifty soundings were randomly chosen to compare to the reanalysis data. The observed LS lapse rate and N^2 values were compared to those derived from the reanalysis data. The LS was defined here as 200–75 hPa. This layer was chosen for two reasons. First, this layer provides a constant analysis layer when the 50 hPa layer used in the actual analysis goes beyond the upper bounds of observed radiosonde data, making an accurate comparison difficult. Secondly, this bound covers 99% of MERRA-2 tropopause pressures, making it a representative layer for the LS environment. Both lapse rate ($R = 0.91$, $P = 8.90e^{-20}$) and N^2 ($R = 0.91$, $P = 1.31e^{-19}$) exhibit good agreement in this layer between the observed and reanalysis data (Fig. 4), indicating that MERRA-2 can represent salient characteristics of the LS environment for use in this study.

4 OT Population

4.1 Location of OTs and OT Characteristics

Before analyzing how LS static stability impacts OTs, understanding spatiotemporal trends of the OT population in SESA is needed. Separating out population level characteristics may help explain the relationship between the LS and OT characteristics. Tracks within 0.02° of the domain edge were removed. Figure 1 shows the spatial groupings of OT tracks. The first large cluster of tracks move off the Sierras de Córdoba mountains and then largely northeast. A second cluster originates and ends southeast of the mountain range between 33° to 34° S and 64° to 63° W (Fig. 1). A third cluster exists to the far northeast of the study domain between 32° to 30° S and 62° to 61° W. These three main areas of OT activity signify where storms with mature, intense updrafts occurred and were likely capable of producing hazardous convective weather.

The location of the maximum OTA and OTD for each OT track are shown in Figures 5a and 5b, respectively. There is no distinct geographical preference in the location of the largest OTs. For example, the very large OTs ($OTA > 200 \text{ km}^2$) are distributed across the study domain. There is a slight tendency for smaller OTs to occur west of the Sierras de Córdoba mountains, and larger OTs to occur east of the mountains over the plains region. This is perhaps related to the means of deep convection initiation, as discussed by Connor Nelson et al. (2022) and Marquis et al. (2021, 2023).

There are, however, geographical preferences in the locations of the deepest OTs. There is a large cluster of the deepest OTs southeast of the mountains from 32.5° to 33.5° S and 64° to 63° W (Fig. 5b). To the south and north of this cluster there are some of the shallowest OTs, with depths around or below 1 km. Deep OTs are also seen to the west of the mountains, in a location found by Mulholland et al. (2018) to be dominated by the initiation of unorganized multicellular convective storms.

4.2 Diurnal Variability

Figure 6 shows the diurnal cycle of OTs during RELAMPAGO-CACTI, normalized by the number of satellite scenes. The bimodal distribution largely follows the expected diurnal cycle of convection. There is a minimum in activity into the morning hours after 05 UTC (02 AM LT) until activity increases again in the afternoon after 15 UTC (12 PM LT). The peak in OT activity occurs at 02 UTC (11 PM LT). This cycle is different than the diurnal cycle observed by GPM in Liu and Liu (2016), but this could be due to differences in times observed or the tropopause definitions used in each study. It is possible some OTs in the early morning hours were missed because there are fewer MDS scans from those times, leading to a sampling bias relative to other hours of the day. We also caution broader interpretation of these results given the limited study period of 4 months.

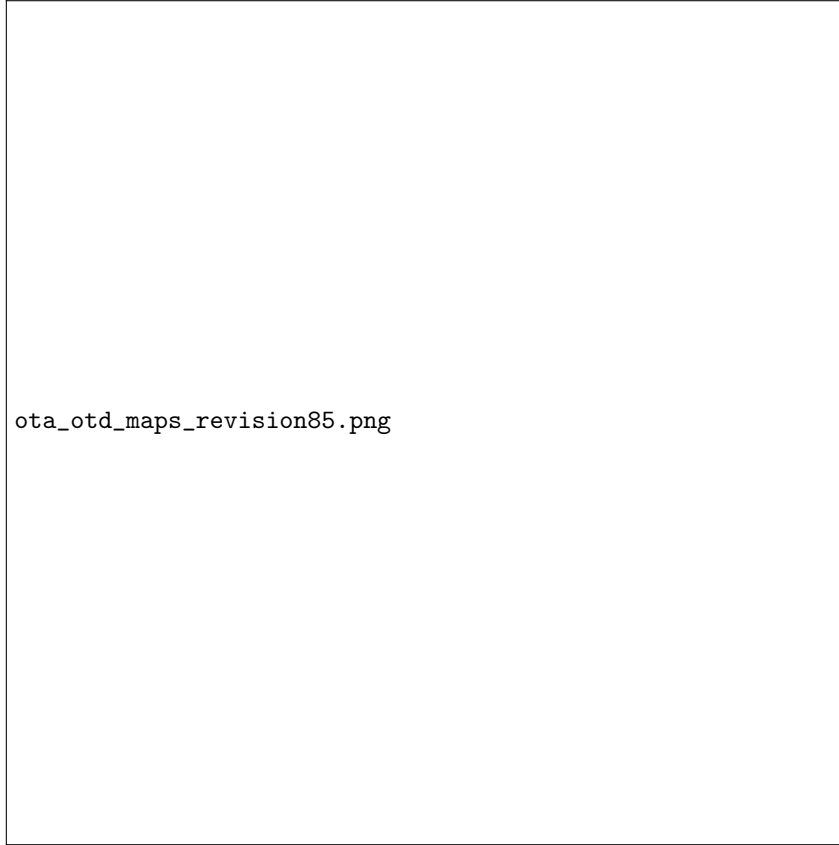


Figure 5. Topographical map showing the location of the maximum OTA a) and maximum OTD b) for the tracks, shaded by OTA and OTD in a) and b), respectively.

Figure 7a shows how $\overline{\text{OTA}}$, where the overbar indicates track-mean values, per OT track varies over the UTC hour of the day. Over the entire day, the median of these values remains around 50 km^2 , largely unaffected by the diurnal cycle. When examining outliers, there may be some impact of the diurnal cycle on $\overline{\text{OTA}}$, however. $\overline{\text{OTA}}$ above 150 km^2 is only seen from 18-05 UTC (01 PM-02 AM LT). The majority of these occur from 01-06 UTC (10 PM-03 AM LT), coinciding with the peak in OT activity and diurnal peak in convection. The shift to the night/overnight hours may indicate how OTA relates to convective mode (i.e. OTA in mesoscale convective systems (MCS) may be larger than in discrete storms), but more work is needed to determine how convective mode and OT characteristics relate.

In contrast, the impact of the diurnal cycle on $\overline{\text{OTD}}$ per OT track is more apparent. The median of these values across all tracked OTs is largest in the overnight hours from 00-05 UTC (09 PM-02 AM LT). The deepest overshoots (around 2.75 km) occur from 00-05 UTC (09 PM-02 AM LT). The trend shown in Figure 7b is consistent with the studies using proxies for convective activity such lightning data from RELAMPAGO (Lang et al., 2020).

Beyond the diurnal trends, OT activity was also examined on a monthly basis. Table 1 shows the $\overline{\text{OTA}}$ and $\overline{\text{OTD}}$ for each month of the study. $\overline{\text{OTA}}$ values are similar but increasing every month. These differences in monthly means may also hint at the role that convective mode may play in OT characteristics. Mulholland et al. (2018) describes the seasonality of convective type in SESA, with austral spring (October-December) tend-

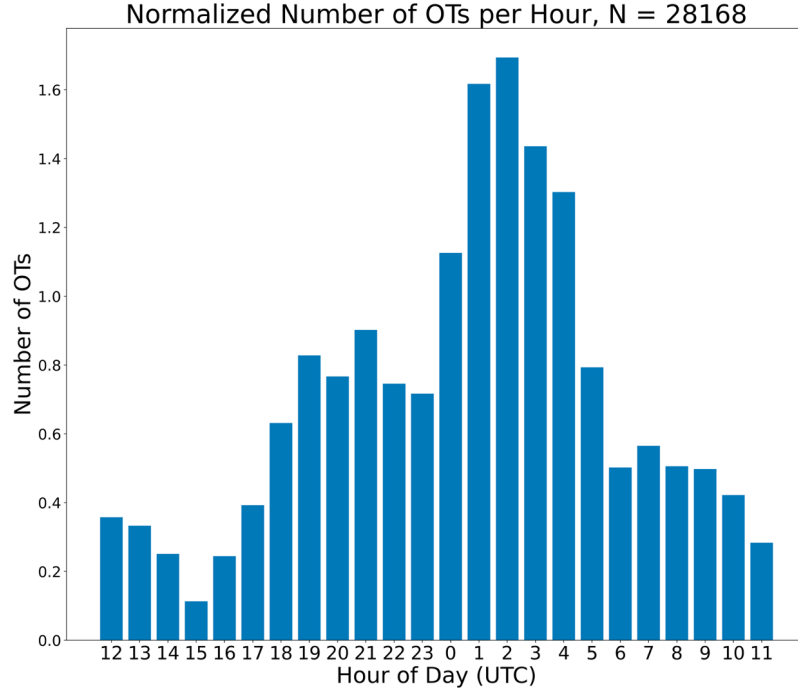


Figure 6. Histogram of the number of detected OTs, i.e. untracked, per hour for the study period, normalized by the number of satellite scenes from each hour.

ing to have more discrete convection, compared to austral summer tending to have more multicell convection. As mentioned above, the differences in updrafts and other differences in convection may play a role in how OT characteristics change seasonally or with different storm modes. $\overline{\text{OTD}}$ exhibits similar variability to $\overline{\text{OTA}}$, but does not follow the same increasing trend. December has the tallest mean overshoots, while January has the shortest mean overshoots.

Table 1. Monthly $\overline{\text{OTA}}$ and $\overline{\text{OTD}}$

	$\overline{\text{OTA}}$ (km ²)	$\overline{\text{OTD}}$ (km)
November	48.99	1.09
December	51.82	1.17
January	53.03	1.07
February	53.47	1.12

5 LS static stability and Observed OT Characteristics

Before assessing the influence of LS static stability on OT characteristics, $\overline{\text{OTA}}$, $\overline{\text{OTD}}$ and $\overline{\text{OTT}}$ of each tracked OT were inter-compared to determine if they were coupled. Figure 8 shows the distributions for OTA , OTD and OTT for each track. Also shown are violin plots for the binned characteristics.

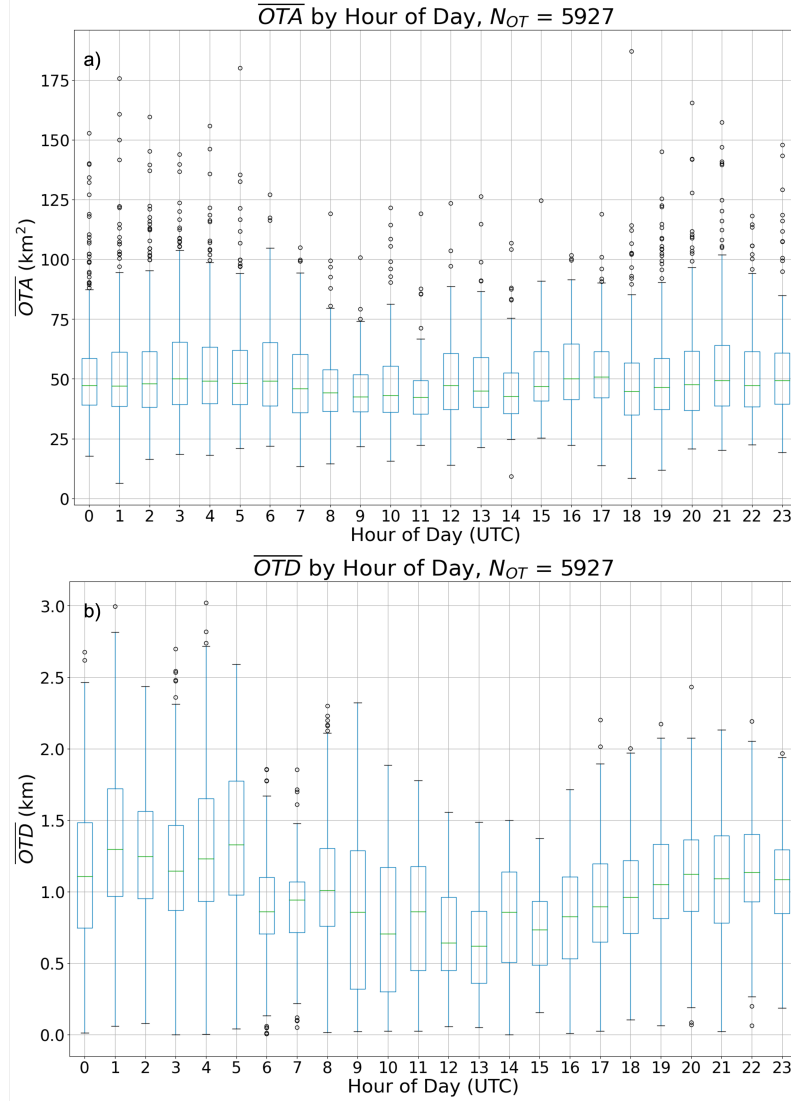


Figure 7. Boxplot showing \overline{OTA} a) and \overline{OTD} b) as a function of hour of the day (UTC)

Figure 8a shows a weak, positive correlation between \overline{OTA} and \overline{OTD} ($R = 0.15$, $P = 2.30e^{-30}$). Most OTs, have a wide range of \overline{OTD} (0.5-2.5+ km) for a relatively narrow range of \overline{OTAs} (25-75 km^2). When examining the medians of the binned distributions, there is an increasing trend, indicating that wider OTs may be linked to taller OTs. \overline{OTA} and \overline{OTT} have a weak, positive correlation ($R = 0.12$, $P = 3.24e^{-20}$). Most OTs are fairly short lived (Fig. 8b), and can still have a wide range of \overline{OTA} . The generally increasing trend of the median values of binned data suggest that wider OTs may also persist longer. \overline{OTT} and \overline{OTD} have a weak, positive correlation ($R = 0.10$, $P = 7.01e^{-15}$). However, there is no clear trend across the binned data, indicating that longer lived OTs are not necessarily taller. To understand potential controls on \overline{OTA} , \overline{OTD} and \overline{OTT} , the relationship between these characteristics to LS static stability is next explored.

\overline{OTA} appears to be not related to LS stability. Figures 9a and 9d show a weak relationship between \overline{OTA} and $\overline{\Gamma}$ ($R = -0.03$, $P = 5.78e^{-1}$) and $\overline{N^2}$ ($R = 0.03$, $P = 1.60e^{-2}$). This suggests that OTA is controlled primarily by updraft-core area below storm top, as hypothesized by Trapp et al. (2017). This is also supported by the absence of a trend

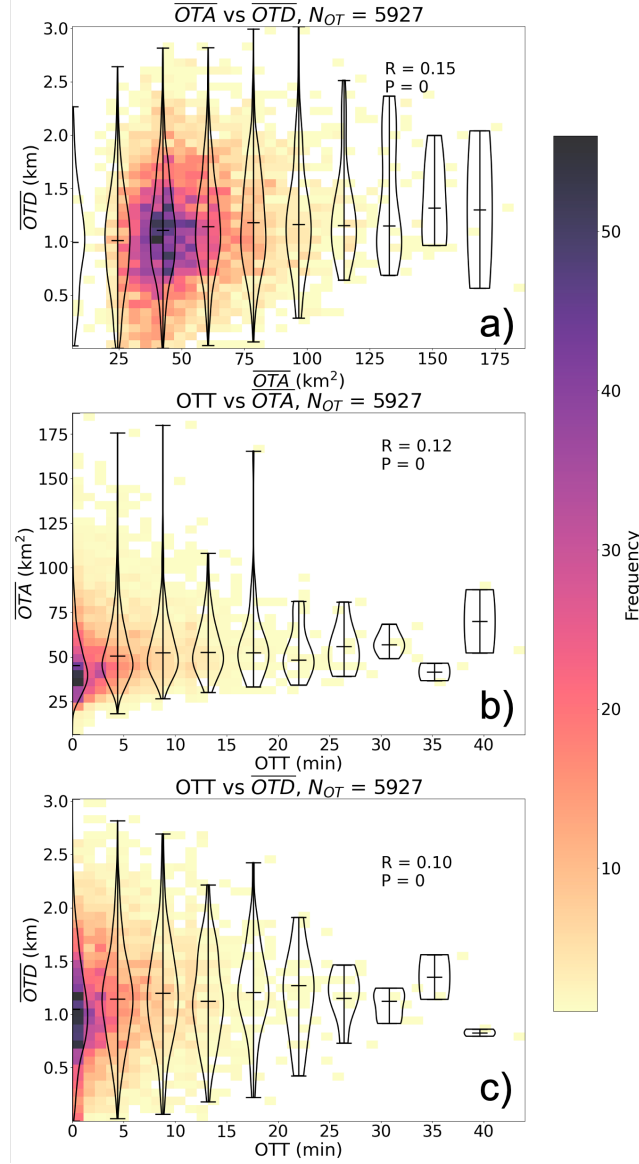


Figure 8. As in Fig. 2 but for $\overline{OTA}/\overline{OTD}$ a), OTT/\overline{OTA} b) and OTT/\overline{OTD} c).

in the binned data, in other words, there is little change in the median values of OTA in the violin plots for increasing values of either $\overline{\Gamma}$ or $\overline{N^2}$. The lack of a relationship between OTA and LS stability has some potentially important implications for extrapolating mid- and low-level storm characteristics from storm-top or satellite-observed features.

In contrast, \overline{OTD} does appear to be somewhat related to LS static stability. Figure 9b shows a moderate, positive correlation between \overline{OTD} and $\overline{\Gamma}$ ($R = 0.38$, $P = 9.94e^{-205}$). This indicates that as lapse rate increases and the LS becomes relatively less stable, \overline{OTD} may increase. Figure 9e shows a moderate, negative linear relationship between \overline{OTD} and $\overline{N^2}$ ($R = -0.37$, $P = 2.61e^{-187}$), a complementary result to that shown in Figure 9b. As $\overline{N^2}$ increases, and thus static stability in the LS increases, the \overline{OTD} will typically decrease. These represent the strongest correlation coefficient values in the study outside of Figure 2, and are supported by the trends in the binned data. As the median

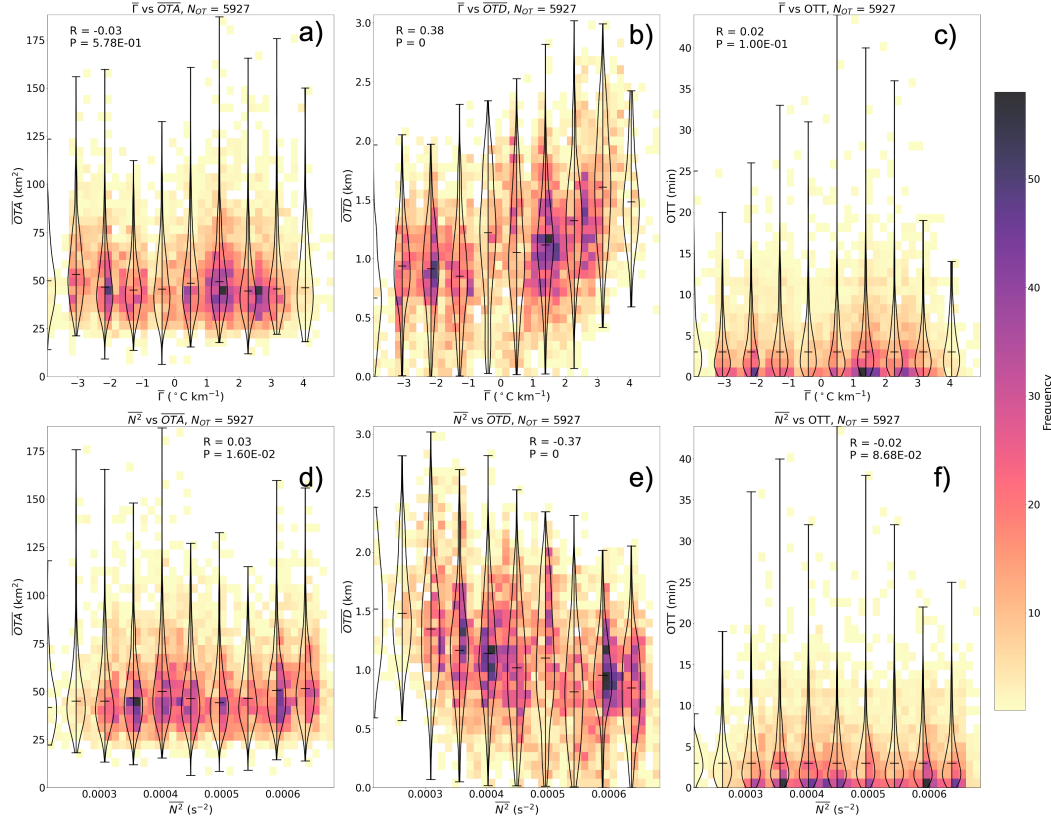


Figure 9. As in Fig. 8, but for \bar{F} a) -c) and \bar{N}^2 d) - f).

values of \bar{F} increase, there is a corresponding increase in \overline{OTD} . A decrease in the median value of binned \overline{OTD} is also seen for increasing values of binned \bar{N}^2 . When taken together, these relationships support OTD being impacted by LMS static stability, where more stable environments lead to shorter OTs.

OTT is weakly correlated to \bar{F} ($R = 0.02$, $P = 1.00e^{-1}$, Fig. 9c) and \bar{N}^2 ($R = -0.02$, $P = 8.68e^{-2}$, Fig. 9f). The trends in the median values for the binned data also show little change for both \bar{F} and \bar{N}^2 , supporting a lack of influence of LMS static stability on OTT. Similar to OTA, updraft characteristics potentially control OTT. An updraft needs a minimum strength to be able to overshoot the high static stability at the tropopause, and thus, the time that the updraft is at that strength is reflected in the duration of the OT. This result is somewhat sensitive to the memory chosen in the tracking algorithm (here 2 minutes). The weak relationships between OTT and LS static stability may provide the ability to extrapolate mid- and low-level storm characteristics from storm-top or satellite-observed features.

To further explore the controls on OT characteristics and to determine whether non-LS environmental parameters can modify OT behavior, \overline{OTA} , \overline{OTD} and OTT were compared to MUCAPE. Figure 10a shows a weak, positive correlation between MUCAPE and \overline{OTA} ($R = 0.11$, $P = 5.10e^{-17}$). There is a positive trend when examining the medians of the binned distributions, indicating more CAPE may be related to larger OTA values. More CAPE is generally expected to lead to wider updrafts, leading to larger OTA values (see Fig. 8a, Lin and Kumjian (2021) and Fig. 10a, Marion and Trapp (2019)). A weak, positive correlation exists between MUCAPE and \overline{OTD} ($R = 0.10$, $P = 6.41e^{-14}$). There is no apparent trend in the median of the binned data, as shown by the violin plots,

indicating that environments with more MUCAPE may not lead to taller OTs. OTT and MUCAPE have a weak, negative correlation ($R = -0.06$, $P = 8.70e^{-6}$). This suggests that an environment of high CAPE does not necessarily lead to a long-lived OT and associated convective storm (Coniglio et al., 2010), and is supported by the lack of trend across the violin plots.

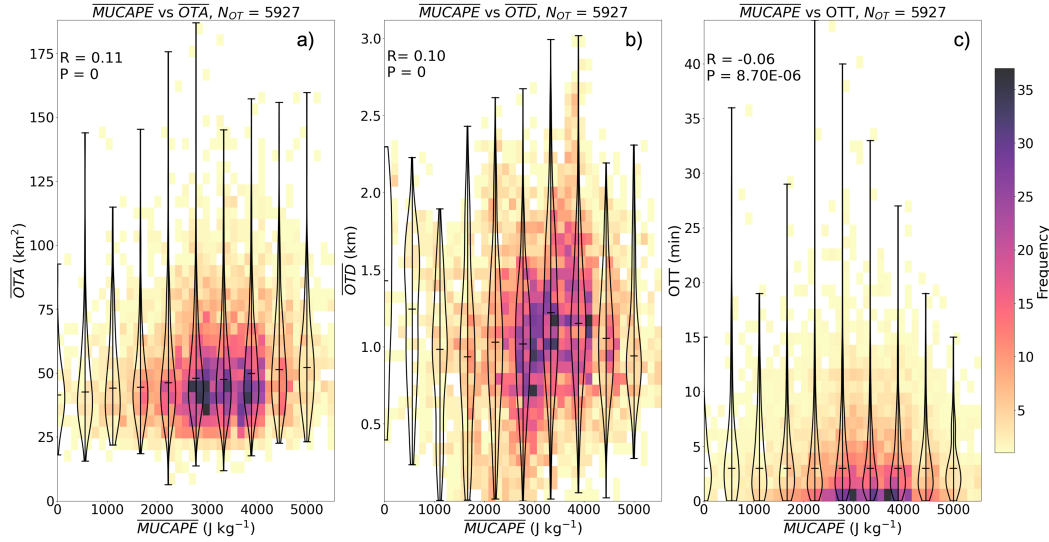


Figure 10. As in Fig. 8, but for $\overline{\text{MUCAPE}}$.

Figure 11 shows how the OT characteristics vary with $\overline{\text{MUCAPE}}$ and LS static stability. The clearest relationship between these linked parameters is for OTD (Fig. 11b, e). The tallest OTs (yellow shading) occur in a less stable LS (positive $\bar{\Gamma}$, smaller \bar{N}^2 values) and tropospheric environments with more CAPE. This signifies that for similar values of CAPE (and potentially updraft strength) OTs in a less stable LS will be able to overshoot more. Both OTA (Fig. 11a, d) and OTT (Fig. 11c, f) show no clear relationship when linking MUCAPE and LS static stability values. There is a slight preference for larger OTA with more CAPE across the LS static stability parameters, showing the influence of updraft characteristics on OTA.

6 Summary and Discussion

This study represents a novel examination of OT occurrence statistics in SESA and of the relationship between LS static stability and the area, depth and duration of a nearby OT. A combination of observed OT characteristics from GOES-16 1-minute MDS data and MERRA-2 reanalysis data were used to derive thermodynamic profiles related to tracked OTs.

OT population analyses show three main clusters of OTs across the study domain, but the widest OTs can happen anywhere across the domain. Maximum OTD, however, shows a spatially varying pattern, with the tallest OTs occurring in a cluster 33° to 34° S and 64° to 63° W over the plains southeast of the Sierras de Córdoba and with additional cross-domain tracks of tall OTs. Temporal trends reveal that while median OTA values do not have a diurnal cycle, the largest OTAs and OTDs do show some influence of a diurnal cycle. OTA also increases monthly, while OTD does not, but both characteristics have similar values across all months.

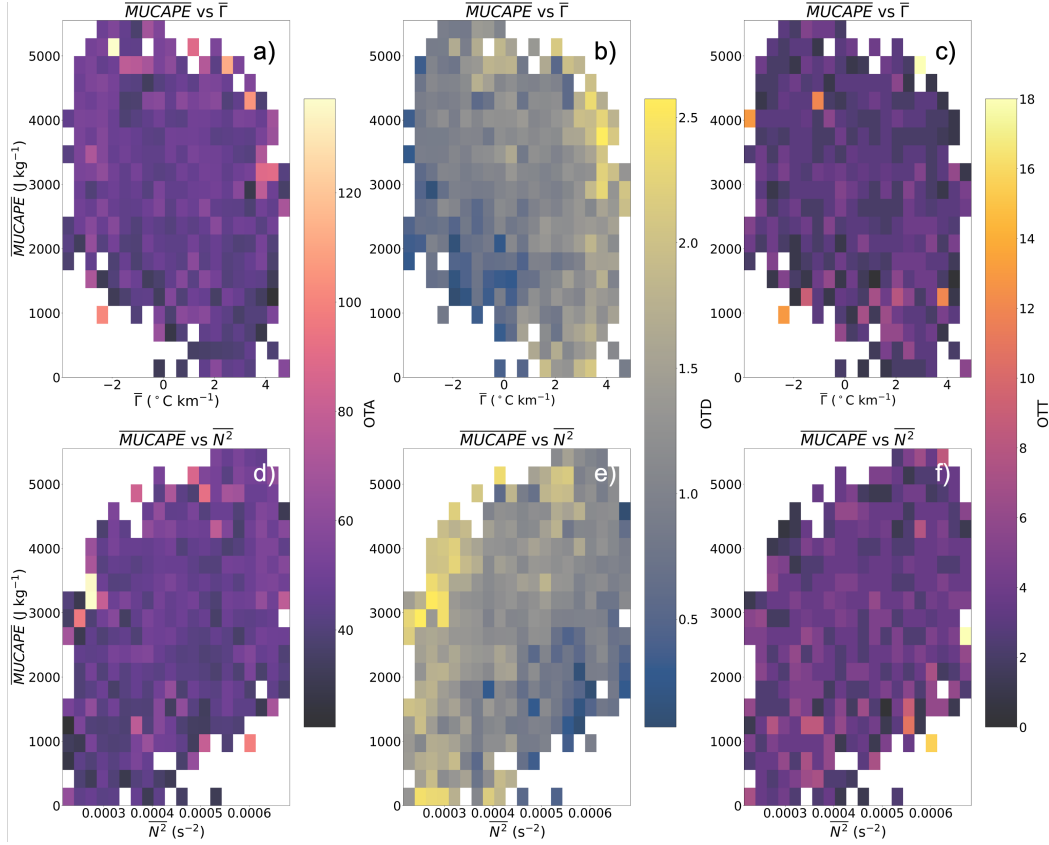


Figure 11. 2D histogram showing $\overline{\text{MUCAPE}}$ and $\overline{\Gamma}$ (a-c), $\overline{N^2}$ (d-f). The histogram boxes are shaded by the median OTA (a, d), median OTD (b, e) and median OTT (c,f) for each bin.

Results show that $\overline{\text{OTA}}$ and $\overline{\text{OTD}}$ are weakly, positively correlated ($R = 0.15$) as are $\overline{\text{OTA}}$ and $\overline{\text{OTT}}$ ($R = 0.12$) and $\overline{\text{OTD}}$ and $\overline{\text{OTT}}$ ($R = 0.10$). When binning the data and examining trends in the median value of each bin, positive trends are found, implying that wider OTs may tend to be taller and persist longer, however longer duration OTs do not necessarily correspond to taller OTs. $\overline{\text{OTA}}$ is weakly correlated to $\overline{\Gamma}$ and $\overline{N^2}$ in the LS ($R = -0.03, 0.03$, respectively), supported by a corresponding lack of trend in the binned data. In contrast, $\overline{\text{OTD}}$ is moderately correlated ($R = 0.38, -0.37$ for $\overline{\Gamma}$ and $\overline{N^2}$, respectively) to static stability in the LS, where increasing static stability leads to decreased OT depths predicted by Eq. 1, supported by the trends in binned data and hypothesized herein and in previous studies (Homeyer et al., 2014b; D. L. Solomon et al., 2016; Gordon & Homeyer, 2022). $\overline{\text{OTT}}$ is weakly correlated to $\overline{\Gamma}$ ($R = 0.02$) and $\overline{N^2}$ ($R = -0.02$).

If observed OTA is largely unaffected by LS static stability, OTA could reasonably be used to derive mid-level updraft area. OTA could predict lower-level storm behavior and potentially ongoing tornado intensity, especially when combined with radar-derived differential reflectivity (Z_{DR}) columns (French & Kingfield, 2021) or OTA's co-evolution with mesocyclone characteristics (Sessa & Trapp, 2020, 2023). This could greatly impact nowcasting for severe convective hazards. Storms with hard to detect low-level rotation, but with robust OTs, may provide additional confidence to forecasters that there is an imminent threat of a convective hazard. On the other hand, forecasters should account for LS static stability before applying OTD for hazardous weather nowcasting.

Beyond these nowcasting implications, OTD and its relationship to LS static stability can impact the amount of water vapor and other mass lofted into the stratosphere via OTs. Dauhut et al. (2018) highlights the role of OTD in the amount of water vapor transported into the stratosphere while Gordon and Homeyer (2022) shows little influence of LS static stability on CTT. Because OTD is tied to static stability in the LS, calculating static stability parameters may be important to mass calculations as static stability in the LS can modify the vertical extent of OTs.

However, much work remains to be done to enhance our knowledge of OTs and their role in the climate system. Recent work has extended the population characteristics component of this work beyond the RELAMPAGO data and SESA (see Cooney et al. (2018); Hong et al. (2023), Jellis et al. (2023)). Hong et al. (2023) also used polar-orbiting satellite data rather than geostationary data to determine long-term trends in OT activity. One aspect missing from much of the previous work is how storm mode can impact the trends seen in this work. Trends may differ when comparing supercell OTs to OTs produced by an MCS or unorganized/mixed-mode convection. These can also be related to the hazards that the different storm modes produce to understand if there is any relationship between convective hazards and specific OT characteristics, extending work such as Marion et al. (2019).

Modeling can be used to further untangle the relationships examined herein. First, high-resolution cloud-resolving model experiments could test the robustness of the relationships further. An ensemble of models would be insightful to diagnose how changing various aspects of LS static stability or updraft characteristics impacts observed OT characteristics. How OTs impact the static stability of the LS can also be examined using models. The transport of water vapor into the LS by OTs may change the temperature and dew point profiles, affecting the static stability (Homeyer, 2015; Johnston et al., 2018; Kuang & Bretherton, 2004). Many of these studies focus on the tropical tropopause layer, however, so detailed examination of the midlatitude tropopause layer is needed. If subsequent OTs occur in the environment, they might have a different depth than would otherwise occur if the OT happened without the environmental modification.

7 Open Research

All MERRA-2 data are publicly available: 3-hourly environmental data ((Global Modeling and Assimilation Office (GMAO), 2015b), doi:10.5067/WWQXQ8IVFW8) and 1-hourly tropopause data, (Global Modeling and Assimilation Office (GMAO), 2015a), doi:10.5067/3Z173KIE2TPD). OT satellite data are available at https://adc.arm.gov/discovery/#/results/id::cor1goecnv2X1.a1.ir.brightness.temperature.lwbroad_goes_satellite?dataLevel=a1&showDetails=true, (Bedka & Khlopenkov, n.d.). Sound-ing data from RELAMPAGO-CACTI can be found at <https://doi.org/10.26023/EXZJ-XBEV-KV05>, (UCAR/NCAR - Earth Observing Laboratory, 2020). Code to derive LS static stability parameters, reconstruct MERRA-2 profiles, track OTs and process the data can be found at https://github.com/mberman99/OT_codes.

Acknowledgments

We are grateful to Max Grover (Argonne National Lab), Yulan Hong (University of Maryland), Alfonso Ladino and Eddie Wolff (University of Illinois Urbana-Champaign) for their feedback and advice on this work. We are also grateful to Kris Bedka (NASA Langley Research Center) for providing us with the satellite data used in this study. Computational support for this study was provided by the UIUC SESE IT staff. Observational data for this study were collected by the RELAMPAGO-CACTI campaign; we are grateful to all who helped with data collecting and processing. We are grateful to the two anonymous reviewers for their feedback on this work. This work is funded by the NASA Grant Number 80NSSC20K0902. Melinda T. Berman was supported by a NASA

FINESST grant Grant Number 80NSSC22K1547. The authors declare no conflicts of interest.

References

- Adler, R. F., & Fenn, D. D. (1979). Thunderstorm intensity as determined by satellite data. *Journal of Applied Meteorology*, 18, 502–517. doi: [https://doi.org/10.1175/1520-0450\(1979\)018<0502:TIADFS>2.0.CO;2](https://doi.org/10.1175/1520-0450(1979)018<0502:TIADFS>2.0.CO;2)
- Adler, R. F., Markus, M. J., Fenn, D. D., Szejwach, G., & Shenk, W. E. (1983). Thunderstorm Top Structure Observed by Aircraft Overflights with an Infrared Radiometer. *Journal of Applied Meteorology and Climatology*, 22(4), 579–593. doi: [10.1175/1520-0450\(1983\)022<0579:TTSOBA>2.0.CO;2](https://doi.org/10.1175/1520-0450(1983)022<0579:TTSOBA>2.0.CO;2)
- Allen, D. B., Caswell, T., Keim, N. C., van der Wel, C. M., & Verweij, R. W. (2023). *Soft-matter/trackpy: V0.6.1*. Zenodo. doi: <https://doi.org/10.5281/zenodo.7670439>.
- Bedka, K., & Khlopenkov, K. (n.d.). *Geostationary Visible and Infrared Imager Deep Convective Storm Detection and Characterization Dataset From NASA Langley Research Center* [Dataset].
- Bedka, K., & Khlopenkov, K. (2016). A probabilistic multispectral pattern recognition method for detection of overshooting cloud tops using passive satellite imager observations. *Journal of Applied Meteorology and Climatology*, 55(9), 1983–2005. doi: [10.1175/JAMC-D-15-0249.1](https://doi.org/10.1175/JAMC-D-15-0249.1)
- Bedka, K., Murillo, E. M., Homeyer, C. R., Scarino, B., & Mersiovsky, H. (2018). The above-anvil cirrus plume: an important severe weather indicator in visible and infrared satellite imagery. *Weather and Forecasting*, 33(5), 1159–1181. doi: [10.1175/WAF-D-18-0040.1](https://doi.org/10.1175/WAF-D-18-0040.1)
- Bernath, P., Boone, C., & Crouse, J. (2022). Wildfire smoke destroys stratospheric ozone. *Science*, 375(6586), 1292–1295. doi: [10.1126/science.abm5611](https://doi.org/10.1126/science.abm5611)
- Birner, T. (2006). Fine-scale structure of the extratropical tropopause region. *Journal of Geophysical Research Atmospheres*, 111(4). doi: [10.1029/2005JD006301](https://doi.org/10.1029/2005JD006301)
- Blumberg, W. G., Halbert, K. T., Supinie, T. A., Marsh, P. T., Thompson, R. L., & Hart, J. A. (2017). Sharppy: an open-source sounding analysis toolkit for the atmospheric sciences. *Bulletin of the American Meteorological Society*, 98(8), 1625–1636. doi: [10.1175/BAMS-D-15-00309.1](https://doi.org/10.1175/BAMS-D-15-00309.1)
- Bosilovich, M. G., Lucchesi, R., & Suarez, M. (2016). *MERRA-2: File Specification. GMAO Office Note No. 9 (Version 1.1)*. GMAO, NASA GSFC.
- Bunkers, M. J., Klimowski, B. A., & Zeitler, J. W. (2002). The importance of parcel choice and the measure of vertical wind shear in evaluating the convective environment. In *21st Conference on Severe Local Storms*. San Antonio, TX. Retrieved from https://ams.confex.com/ams/SLS_WAF_NWP/techprogram/paper_47319.htm
- Coniglio, M. C., Hwang, J. Y., & Stensrud, D. J. (2010). Environmental factors in the upscale growth and longevity of MCSs derived from Rapid Update Cycle analyses. *Monthly Weather Review*, 138(9), 3514–3539. doi: [10.1175/2010MWR3233.1](https://doi.org/10.1175/2010MWR3233.1)
- Connor Nelson, T., Marquis, J., Peters, J. M., & Friedrich, K. (2022). Environmental controls on simulated deep moist convection initiation occurring during RELAMPAGO-CACTI. *Journal of the Atmospheric Sciences*, 79(6). doi: [10.1175/JAS-D-21-0226.1](https://doi.org/10.1175/JAS-D-21-0226.1)
- Cooney, J. W., Bedka, K. M., Bowman, K. P., Khlopenkov, K. V., & Itterly, K. (2021). Comparing tropopause-penetrating convection identifications derived from NEXRAD and GOES over the contiguous united states. *Journal of Geophysical Research: Atmospheres*, 126(14). doi: [10.1029/2020JD034319](https://doi.org/10.1029/2020JD034319)
- Cooney, J. W., Bowman, K. P., Homeyer, C. R., & Fenske, T. M. (2018). Ten

- year analysis of tropopause-overshooting convection using GridRad data. *Journal of Geophysical Research: Atmospheres*, 123(1), 329–343. doi: 10.1002/2017JD027718
- Crocker, J. C., & Grier, D. G. (1996). Methods of digital video microscopy for colloidal studies. *Journal of Colloid and Interface Science*, 179(1), 298–310. doi: 10.1006/jcis.1996.0217
- Dauhut, T., Chaboureau, J. P., Haynes, P. H., & Lane, T. P. (2018). The mechanisms leading to a stratospheric hydration by overshooting convection. *Journal of the Atmospheric Sciences*, 75(12), 4383–4398. doi: 10.1175/JAS-D-18-0176.1
- Di Girolamo, L., & Davies, R. (1997). Cloud fraction errors caused by finite resolution measurements. *Journal of Geophysical Research Atmospheres*, 102(2), 1739–1756. doi: 10.1029/96jd02663
- Dworak, R., Bedka, K., Brunner, J., & Feltz, W. (2012). Comparison between GOES-12 overshooting-top detections, WSR-88D radar reflectivity, and severe storm reports. *Weather and Forecasting*, 27, 684–699. doi: https://doi.org/10.1175/WAF-D-11-00070.1
- Fischer, H., De Reus, M., Traub, M., Williams, J., Lelieveld, J., De Gouw, J., ... Siegmund, P. (2003). Atmospheric Chemistry and Physics Deep convective injection of boundary layer air into the lowermost stratosphere at midlatitudes. *Atmospheric Chemistry and Physics*, 3, 739–745.
- French, M. M., & Kingfield, D. M. (2021). Tornado formation and intensity prediction using polarimetric radar estimates of updraft area. *Weather and Forecasting*. doi: 10.1175/waf-d-21-0087.1
- Fromm, M., Lindsey, D. T., Servranckx, R., Yue, G., Trickl, T., Sica, R., ... Godin-Beekmann, S. (2010). The untold story of pyrocumulonimbus. *Bulletin of the American Meteorological Society*, 91(9), 1193–1209. doi: 10.1175/2010BAMS3004.1
- Fueglistaler, S., Dessler, A. E., Dunkerton, T. J., Folkins, I., Fu, Q., & Mote, P. W. (2009). Tropical tropopause layer. *Reviews of Geophysics*, 47(1). doi: 10.1029/2008RG000267
- Fujita, T. T. (1974). *Overshooting thunderheads observed from ATS and Learjet* (Tech. Rep.). The University of Chicago.
- Fujiwara, M., Manney, G. L., Gray, L. J., & Wright, J. S. (2022). *SPARC Reanalysis Intercomparison Project (S-RIP) Final Report* [Monograph]. (ISSN: 2296-5785 Num Pages: 612) doi: 10.17874/800dee57d13
- Gelaro, R., McCarty, W., Suárez, M. J., Todling, R., Molod, A., Takacs, L., ... Zhao, B. (2017). The modern-era retrospective analysis for research and applications, version 2 (MERRA-2). *Journal of Climate*, 30(14), 5419–5454. doi: 10.1175/JCLI-D-16-0758.1
- Global Modeling and Assimilation Office (GMAO). (2015a). *MERRA-2 inst1_2d_asm_Nx: 2d,1-Hourly,Instantaneous,Single-Level,Assimilation,Single-Level Diagnostics V5.12.4* [Dataset]. Greenbelt, MD, USA: Goddard Earth Sciences Data and Information Services Center (GES DISC). (Last accessed 24 October 2023) doi: 10.5067/3Z173KIE2TPD
- Global Modeling and Assimilation Office (GMAO). (2015b). *MERRA-2 inst3_3d_asm_Nv: 3d,3-Hourly,Instantaneous,Model-Level,Assimilation,Assimilated Meteorological Fields V5.12.4* [Dataset]. Greenbelt, MD, USA: Goddard Earth Sciences Data and Information Services Center (GES DISC). (Last accessed 24 October 2023) doi: 10.5067/WWQSXQ8IVFW8
- Gordon, A. E., & Homeyer, C. R. (2022). Sensitivities of cross-tropopause transport in midlatitude overshooting convection to the lower stratosphere environment. *Journal of Geophysical Research: Atmospheres*, 127(13). doi: 10.1029/2022JD036713

- Grover, M. A. (2021). *Estimating midlevel updraft characteristics and severe weather intensity through the lens of overshooting tops* (Thesis). University of Illinois at Urbana-Champaign.
- Hegglin, M. I., Brunner, D., Wernli, H., Schwierz, C., Martius, O., Hoor, P., . . . Peter, T. (2004). Tracing troposphere-to-stratosphere transport above a mid-latitude deep convective system. *Atmospheric Chemistry and Physics*, 4, 741–756. doi: doi.org/10.5194/acp-4-741-2004
- Herman, R. L., Ray, E. A., Rosenlof, K. H., Bedka, K. M., Schwartz, M. J., Read, W. G., . . . Dean-Day, J. M. (2017). Enhanced stratospheric water vapor over the summertime continental United States and the role of overshooting convection. *Atmospheric Chemistry and Physics*, 17(9), 6113–6124. doi: 10.5194/acp-17-6113-2017
- Heymsfield, G. M., Tian, L., Heymsfield, A. J., Li, L., & Guimond, S. (2010). Characteristics of deep tropical and subtropical convection from nadir-viewing high-altitude airborne doppler radar. *Journal of the Atmospheric Sciences*, 67(2), 285–308. doi: 10.1175/2009JAS3132.1
- Holton, J. R., Haynes, P. H., McIntyre, M. E., Douglass, A. R., Rood, R. B., & Pfister, L. (1995). Stratosphere-troposphere exchange. *Review of Geophysics*, 33(4), 403–439.
- Homeyer, C. R. (2015). Numerical simulations of extratropical tropopause-penetrating convection: Sensitivities to grid resolution. *Journal of Geophysical Research: Atmospheres*, 120(14), 7174–7188. doi: 10.1002/2015JD023356
- Homeyer, C. R., McAuliffe, J. D., & Bedka, K. M. (2017). On the Development of Above-Anvil Cirrus Plumes in Extratropical Convection. *Journal of the Atmospheric Sciences*, 74(5), 1617–1633. doi: 10.1175/JAS-D-16-0269.1
- Homeyer, C. R., Pan, L. L., & Barth, M. C. (2014a). Transport from convective overshooting of the extratropical tropopause and the role of large-scale lower stratosphere stability. *Journal of Geophysical Research*, 119(5), 2220–2240. doi: 10.1002/2013JD020931
- Homeyer, C. R., Pan, L. L., Dorsi, S. W., Avallone, L. M., Weinheimer, A. J., O’Brien, A. S., . . . Campos, T. L. (2014b). Convective transport of water vapor into the lower stratosphere observed during double-tropopause events. *Journal of Geophysical Research*, 119(18), 10,941–10,958. doi: 10.1002/2014JD021485
- Hong, Y., Nesbitt, S. W., Trapp, R. J., & Di Girolamo, L. (2023). Near-global distributions of overshooting tops derived from Terra and Aqua MODIS observations. *Atmospheric Measurement Techniques*, 16(5), 1391–1406. doi: 10.5194/amt-16-1391-2023
- Huntrieser, H., Lichtenstern, M., Scheibe, M., Aufmhoff, H., Schlager, H., Pucik, T., . . . Barth, M. C. (2016). On the origin of pronounced O₃ gradients in the thunderstorm outflow region during DC3. *Journal of Geophysical Research: Atmospheres*, 121(11), 6600–6637. doi: 10.1002/2015JD024279
- Jellis, D., Bowman, K. P., & Rapp, A. D. (2023). Lifetimes of overshooting convective events using high-frequency gridded radar composites. *Monthly Weather Review*, 151(8), 1979–1992. doi: 10.1175/MWR-D-23-0032.1
- Johnston, B. R., Xie, F., & Liu, C. (2018). The Effects of Deep Convection on Regional Temperature Structure in the Tropical Upper Troposphere and Lower Stratosphere. *Journal of Geophysical Research: Atmospheres*, 123(3), 1585–1603. doi: 10.1002/2017JD027120
- Khlopenkov, K. V., Bedka, K. M., Cooney, J. W., & Iterly, K. (2021). Recent advances in detection of overshooting cloud tops from longwave infrared satellite imagery. *Journal of Geophysical Research: Atmospheres*, 126(14). doi: 10.1029/2020JD034359
- Khordakova, D., Rolf, C., Grooß, J.-U., Müller, R., Konopka, P., Wieser, A., . . . Riese, M. (2022). A case study on the impact of severe convective storms on

- the water vapor mixing ratio in the lower mid-latitude stratosphere observed in 2019 over Europe. *Atmospheric Chemistry and Physics*, 22(2), 1059–1079. doi: 10.5194/acp-22-1059-2022
- Kuang, Z., & Bretherton, C. S. (2004). Convective Influence on the Heat Balance of the Tropical Tropopause Layer: A Cloud-Resolving Model Study. *Journal of the Atmospheric Sciences*, 61(23), 2919–2927. doi: 10.1175/JAS-3306.1
- Lane, T. P., Sharman, R. D., Clark, T. L., & Hsu, H.-M. (2003). An investigation of turbulence generated mechanisms above deep convection. *Journal of the Atmospheric Sciences*, 60(10), 1297–1321. doi: 10.1175/1520-0469(2003)60<1297:AIOTGM>2.0.CO;2
- Lang, T. J., Ávila, E. E., Blakeslee, R. J., Burchfield, J., Wingo, M., Bitzer, P. M., ... Pereyra, R. G. (2020). The RELAMPAGO Lightning Mapping Array: overview and initial comparison with the Geostationary Lightning Mapper. *Journal of Atmospheric and Oceanic Technology*. doi: 10.1175/JTECH-D-20
- Lin, Y., & Kumjian, M. R. (2021). Influences of CAPE on hail production in simulated supercell storms. *Journal of the Atmospheric Sciences*, 79(1), 179–204. doi: 10.1175/JAS-D-21-0054.1
- Liu, N., & Liu, C. (2016). Global distribution of deep convection reaching tropopause in 1 year GPM observations. *Journal of Geophysical Research: Atmospheres*, 121(8), 3824–3842. doi: 10.1002/2015JD024430
- Liu, N., Liu, C., & Hayden, L. (2020). Climatology and Detection of Overshooting Convection From 4 Years of GPM Precipitation Radar and Passive Microwave Observations. *Journal of Geophysical Research: Atmospheres*, 125(7), e2019JD032003. (eprint: <https://onlinelibrary.wiley.com/doi/pdf/10.1029/2019JD032003>) doi: 10.1029/2019JD032003
- Marion, G. R., & Trapp, R. J. (2019). The dynamical coupling of convective updrafts, downdrafts, and cold pools in simulated supercell thunderstorms. *Journal of Geophysical Research: Atmospheres*, 124(2), 664–683. doi: 10.1029/2018JD029055
- Marion, G. R., Trapp, R. J., & Nesbitt, S. W. (2019). Using overshooting top area to discriminate potential for large, intense tornadoes. *Geophysical Research Letters*, 46(21), 12520–12526. doi: 10.1029/2019GL084099
- Marquis, J. N., Feng, Z., Varble, A., Nelson, T. C., Houston, A., Peters, J. M., ... Hardin, J. (2023). Near-cloud atmospheric ingredients for deep convection initiation. *Monthly Weather Review*, 151(5), 1247–1267. doi: 10.1175/MWR-D-22-0243.1
- Marquis, J. N., Varble, A. C., Robinson, P., Nelson, T. C., & Friedrich, K. (2021). Low-level mesoscale and cloud-scale interactions promoting deep convection initiation. *Monthly Weather Review*, 149(8), 2473–2495. doi: 10.1175/MWR-D-20-0391.1
- May, R. M., Goebbert, K. H., Thielen, J. E., Leeman, J. R., Drew Camron, M., Bruick, Z., ... Marsh, P. T. (2022). MetPy: a meteorological python library for data analysis and visualization. *Bulletin of the American Meteorological Society*, 103(10), E2273–E2284. doi: 10.1175/BAMS-D-21-0125.1
- Mulholland, J. P., Nesbitt, S. W., Trapp, R. J., Rasmussen, K. L., & Salio, P. V. (2018). Convective storm life cycle and environments near the Sierras de Córdoba, Argentina. *Monthly Weather Review*, 146(8), 2541–2557. doi: 10.1175/MWR-D-18-0081.1
- Negri, A. J. (1982). Cloud-top Structure of Tornadic Storms on 10 April 1979 from Rapid Scan and Stereo Satellite Observations. *Bulletin of the American Meteorological Society*, 63(10), 1151–1159. doi: 10.1175/1520-0477-63.10.1151
- Nesbitt, S. W., Salio, P. V., Ávila, E., Bitzer, P., Carey, L., Chandrasekar, V., ... Grover, M. A. (2021). A storm safari in subtropical South America: Proyecto RELAMPAGO. *Bulletin of the American Meteorological Society*, 102(8),

- E1621–E1644. doi: 10.1175/BAMS-D-20-0029.1
- O’Neill, M. E., Orf, L., Heymsfield, G. M., & Halbert, K. (2021). Hydraulic jump dynamics above supercell thunderstorms. *Science*, *373*, 1248–1251. doi: 10.1126/science.abh3857
- Pan, L. L., Homeyer, C. R., Honomichl, S., Ridley, B. A., Weisman, M., Barth, M. C., . . . Huntrieser, H. (2014). Thunderstorms enhance tropospheric ozone by wrapping and shedding stratospheric air. *Geophysical Research Letters*, *41*(22), 7785–7790. doi: 10.1002/2014GL061921
- Rochette, S. M., Moore, J. T., & Market, P. S. (1999). The importance of parcel choice in elevated CAPE computations. *National Weather Digest*, *23*(4).
- Schmit, T. J., Griffith, P., Gunshor, M. M., Daniels, J. M., Goodman, S. J., & Lebar, W. J. (2017). A closer look at the ABI on the GOES-R Series. *Bulletin of the American Meteorological Society*, *98*(4), 681–698. doi: 10.1175/BAMS-D-15-00230.1
- Schoeberl, M. R., Ueyama, R., & Pfister, L. (2022). A lagrangian view of seasonal stratosphere-troposphere exchange. *Journal of Geophysical Research: Atmospheres*, *127*(16), e2022JD036772. doi: 10.1029/2022JD036772
- Schroeder, J. R., Pan, L. L., Ryerson, T., Diskin, G., Hair, J., Meinardi, S., . . . Blake, D. R. (2014). Evidence of mixing between polluted convective outflow and stratospheric air in the upper troposphere during DC3. *Journal of Geophysical Research: Atmospheres*, *119*(19), 11,477–11,491. doi: 10.1002/2014JD022109
- Sessa, M., & Trapp, R. (2023). Environmental and radar-derived predictors of tornado intensity within ongoing convective storms. *Journal of Operational Meteorology*, 49–71. doi: 10.15191/nwajom.2023.1105
- Sessa, M., & Trapp, R. J. (2020). Observed relationship between tornado intensity and pretornadic mesocyclone characteristics. *Weather and Forecasting*, *35*(4), 1243–1261. doi: 10.1175/WAF-D-19-0099.1
- Setvák, M., Lindsey, D. T., Rabin, R. M., Wang, P. K., & Demeterová, A. (2008). Indication of water vapor transport into the lower stratosphere above midlatitude convective storms: Meteosat Second Generation satellite observations and radiative transfer model simulations. *Atmospheric Research*, *89*(1-2), 170–180. doi: 10.1016/j.atmosres.2007.11.031
- Solomon, D. L., Bowman, K. P., & Homeyer, C. R. (2016). Tropopause-penetrating convection from Three-Dimensional gridded NEXRAD data. *Journal of Applied Meteorology and Climatology*, *55*(2), 465–478. doi: 10.1175/JAMC-D-15-0190.1
- Solomon, S., Rosenlof, K. H., Portmann, R. W., Daniel, J. S., Davis, S. M., Sanford, T. J., & Plattner, G.-K. (2010). Contributions of stratospheric water vapor to decadal changes in the rate of global warming. *Science*, *327*(5970), 1219–1223. doi: 10.1126/science.1182488
- Trapp, R. J., Marion, G. R., & Nesbitt, S. W. (2017). The regulation of tornado intensity by updraft width. *Journal of the Atmospheric Sciences*, *74*(12), 4199–4211. doi: 10.1175/JAS-D-16-0331.1
- UCAR/NCAR - Earth Observing Laboratory. (2020). *Multi-Network Composite 5mb Vertical Resolution Sounding Composite. Version 1.3* [Dataset]. UCAR/NCAR - Earth Observing Laboratory. doi: <https://doi.org/10.26023/EXZJ-XBEV-KV05>
- van der Walt, S., Schönberger, J. L., Nunez-Iglesias, J., Boulogne, F., Warner, J. D., Yager, N., . . . the scikit-image contributors (2014). scikit-image: image processing in python. *PeerJ*, *2*, e453. Retrieved from <https://doi.org/10.7717/peerj.453> doi: 10.7717/peerj.453
- Varble, A. C., Nesbitt, S. W., Salio, P., Hardin, J. C., Bharadwaj, N., Borque, P., . . . Zipser, E. J. (2021). Utilizing a storm-generating hotspot to study convective cloud transitions: The CACTI experiment. *Bulletin of the American Meteor-*

- logical Society, 102(8), E1597–E1620. doi: 10.1175/BAMS-D-20-0030.1
- Virtanen, P., Gommers, R., Oliphant, T. E., Haberland, M., Reddy, T., Cournapeau, D., . . . SciPy 1.0 Contributors (2020). SciPy 1.0: Fundamental Algorithms for Scientific Computing in Python. *Nature Methods*, 17, 261–272. doi: 10.1038/s41592-019-0686-2
- Wang, P. K. (2003). Moisture plumes above thunderstorm anvils and their contributions to cross-tropopause transport of water vapor in midlatitudes. *Journal of Geophysical Research: Atmospheres*, 108(D6). doi: 10.1029/2002JD002581
- Wargan, K., & Coy, L. (2016). Strengthening of the tropopause inversion layer during the 2009 sudden stratospheric warming: a MERRA-2 study. *Journal of the Atmospheric Sciences*, 73(5), 1871–1887. doi: 10.1175/JAS-D-15-0333.1
- Xian, T., & Homeyer, C. R. (2019). Global tropopause altitudes in radiosondes and reanalyses. *Atmospheric Chemistry and Physics*, 19(8), 5661–5678. doi: 10.5194/acp-19-5661-2019
- Zipser, E. J., Cecil, D. J., Liu, C., Nesbitt, S. W., & Yorty, D. P. (2006). Where are the most intense thunderstorms on earth? *Bulletin of the American Meteorological Society*, 87(8), 1057–1072. doi: 10.1175/BAMS-87-8-1057

Figure 1.

All OT Tracks, N = 5927

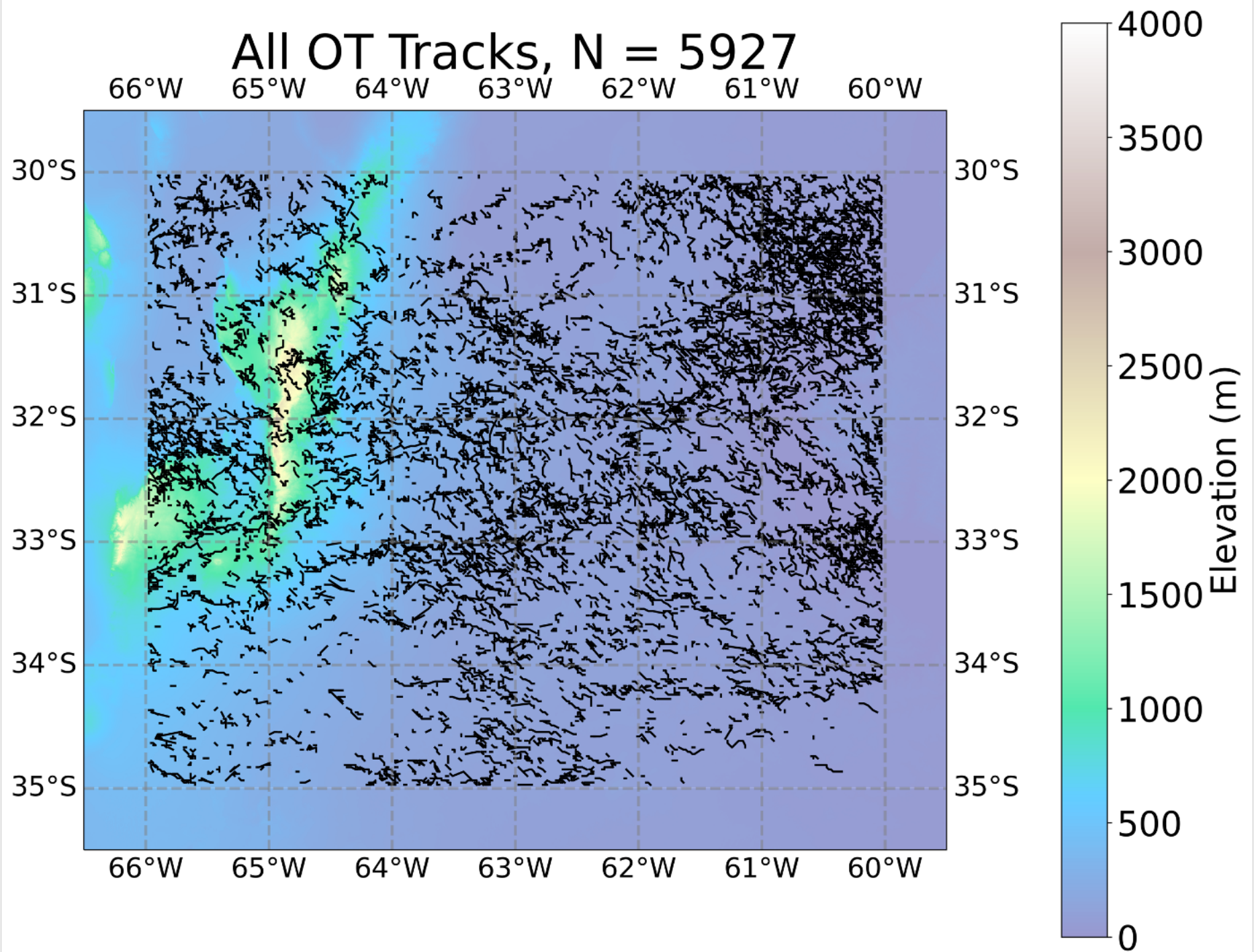


Figure 2.

Track Length vs Track Duration, N = 5927

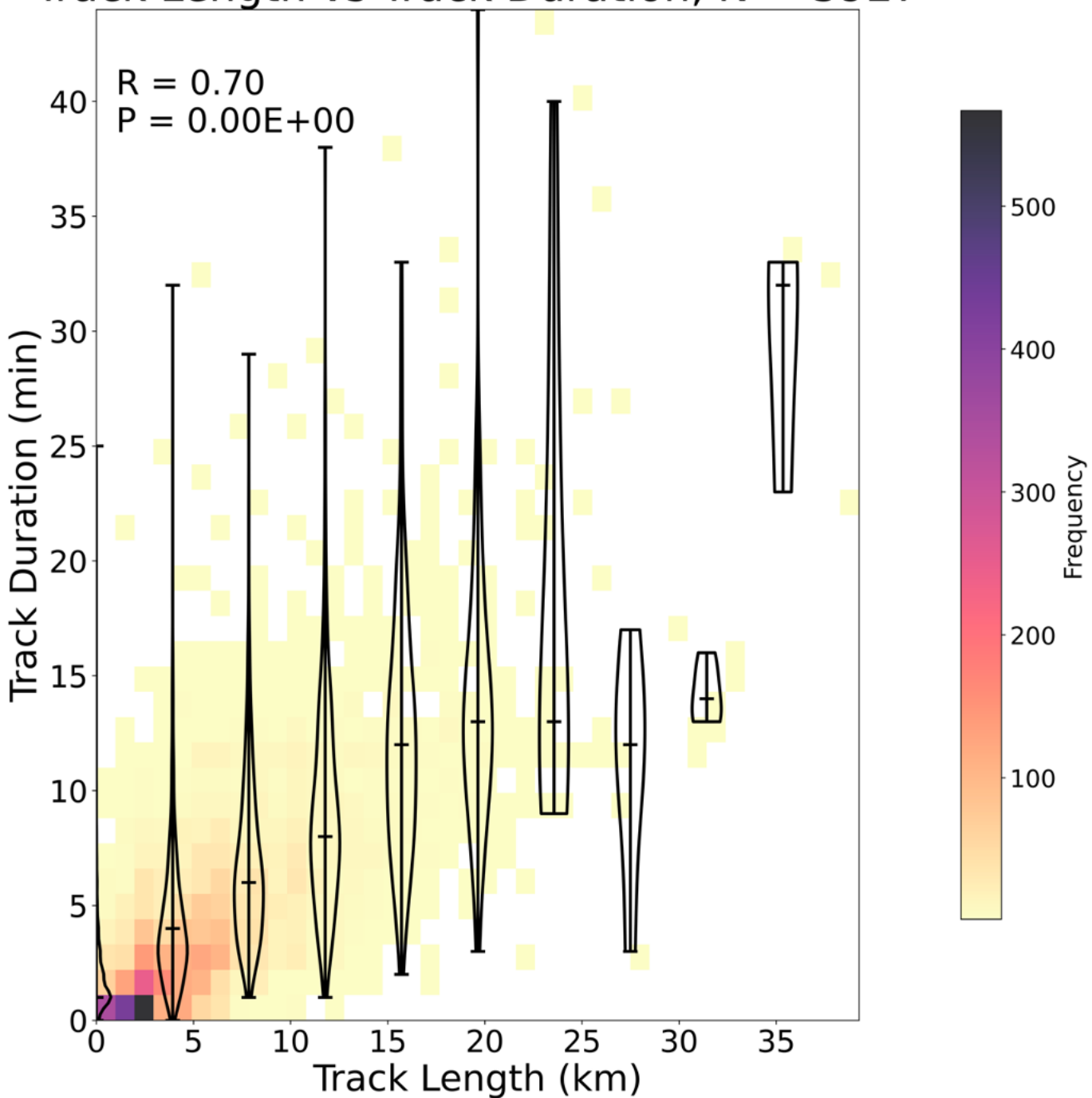


Figure 3.

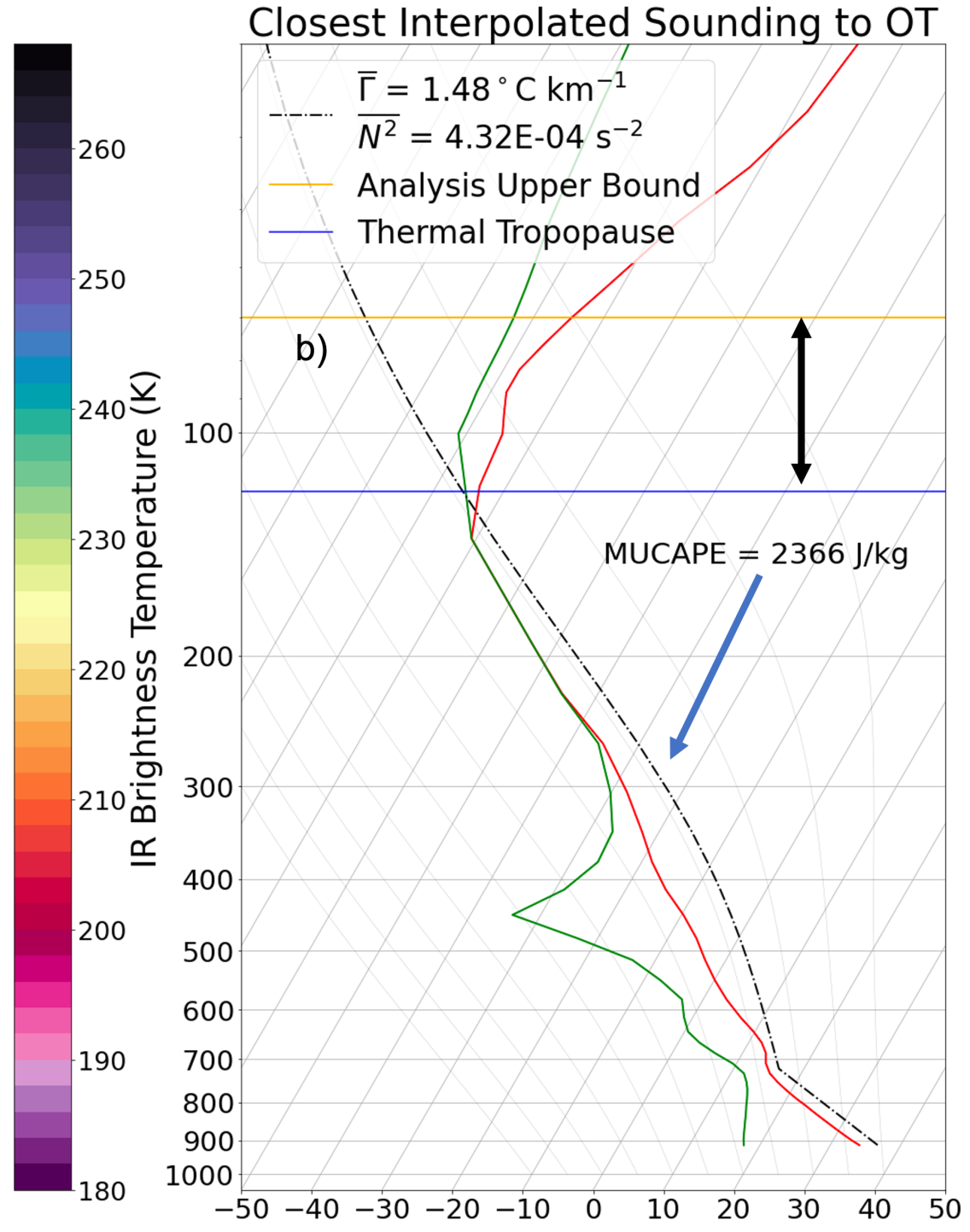
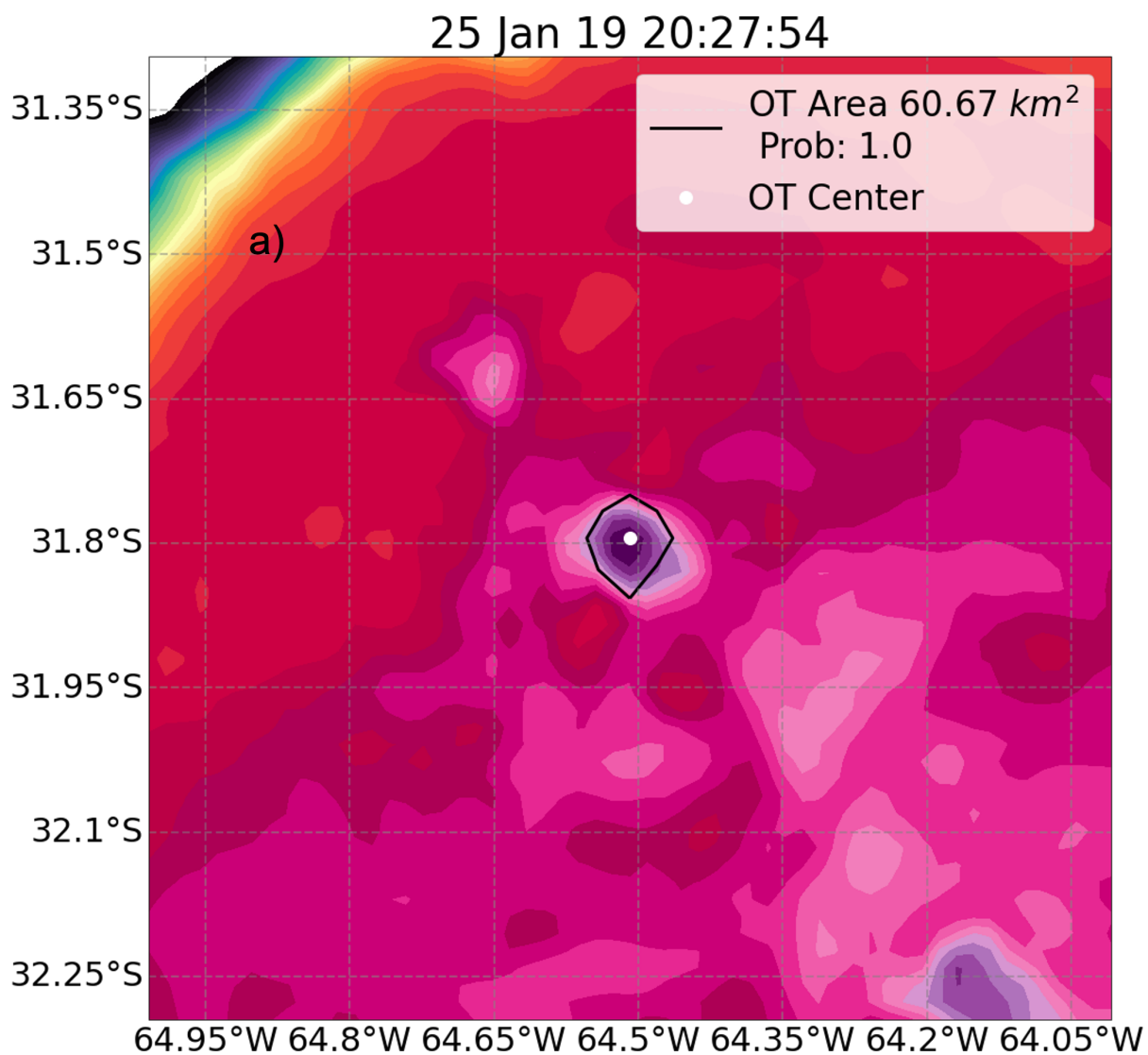


Figure 4.

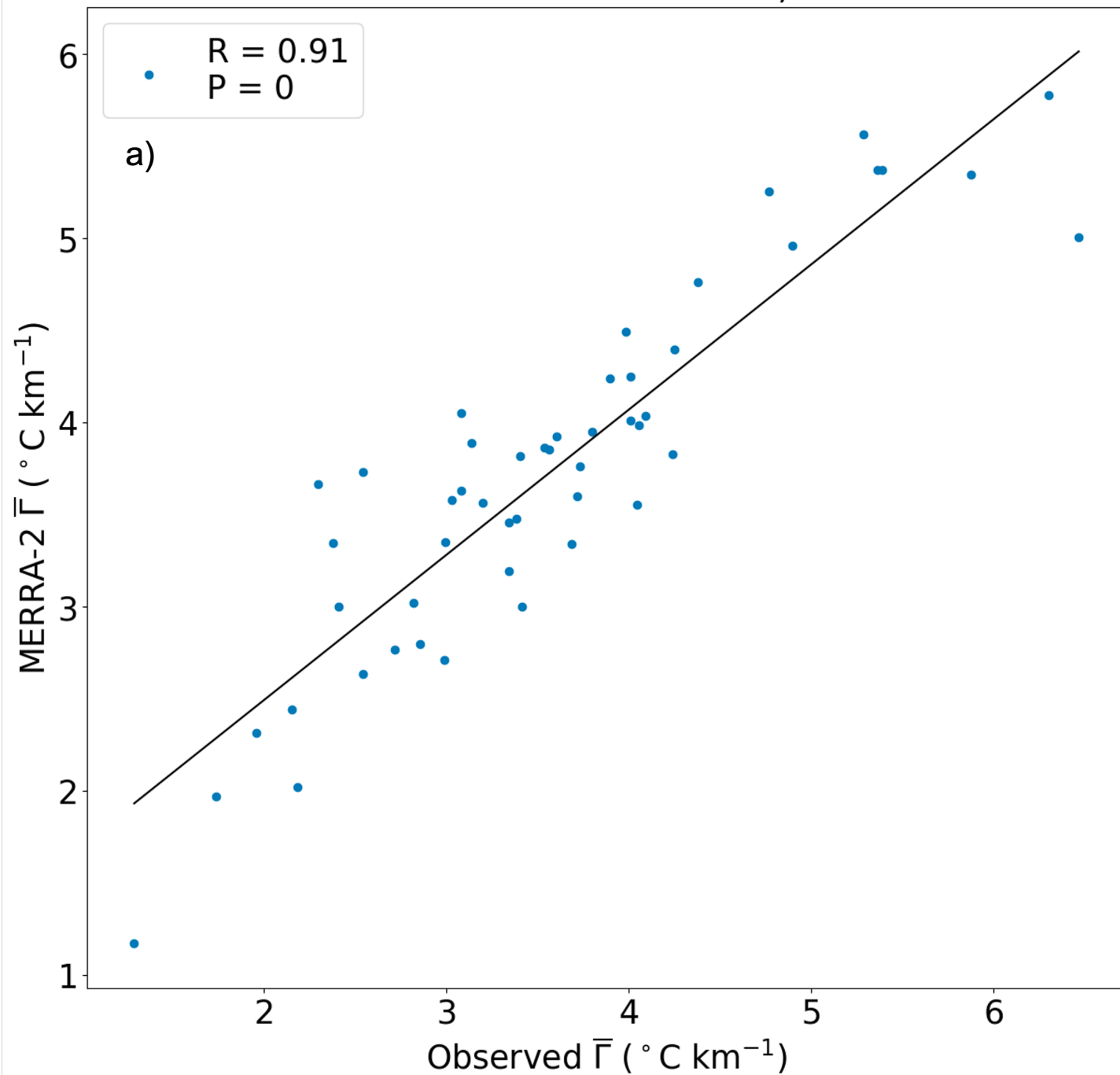
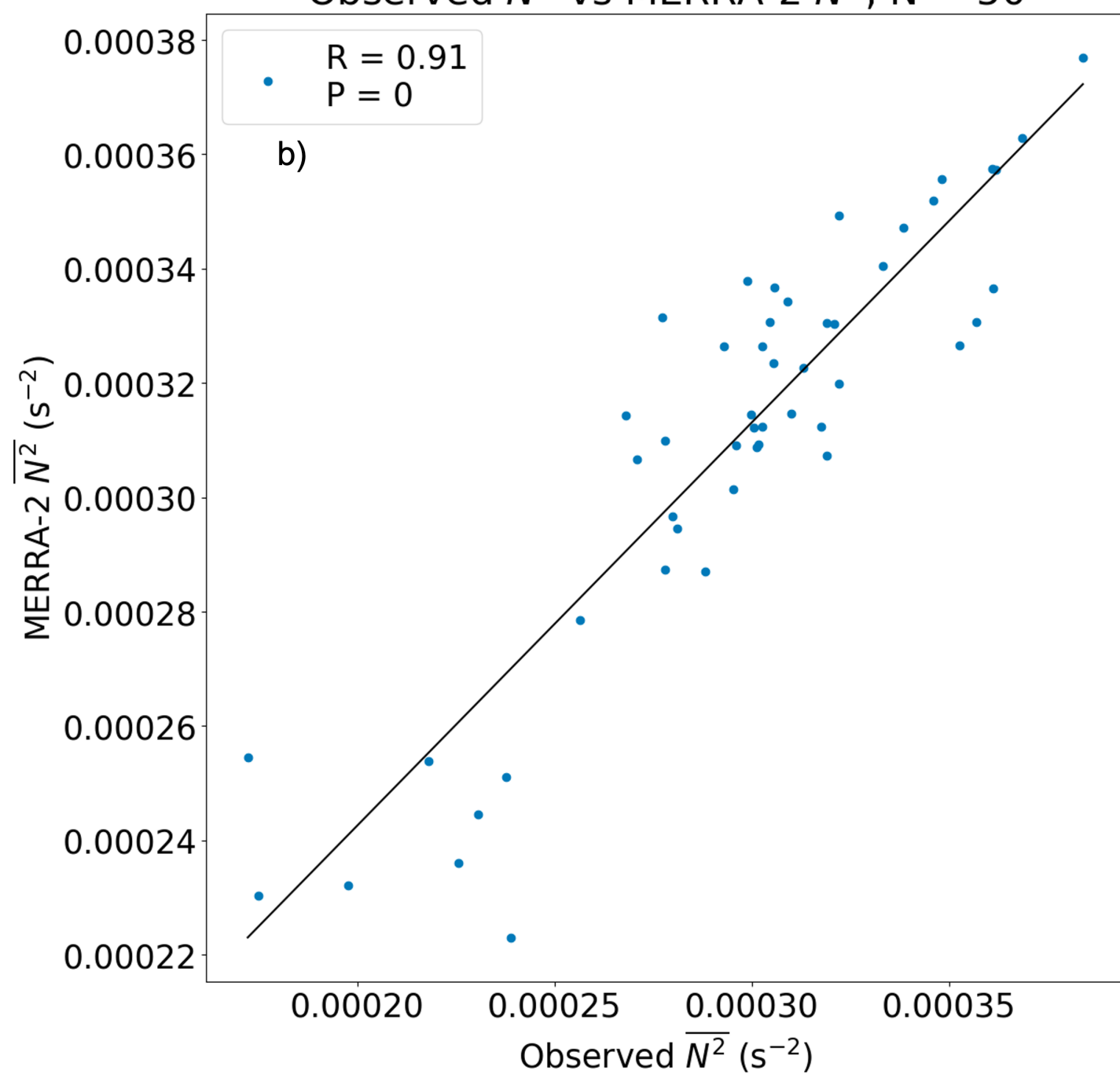
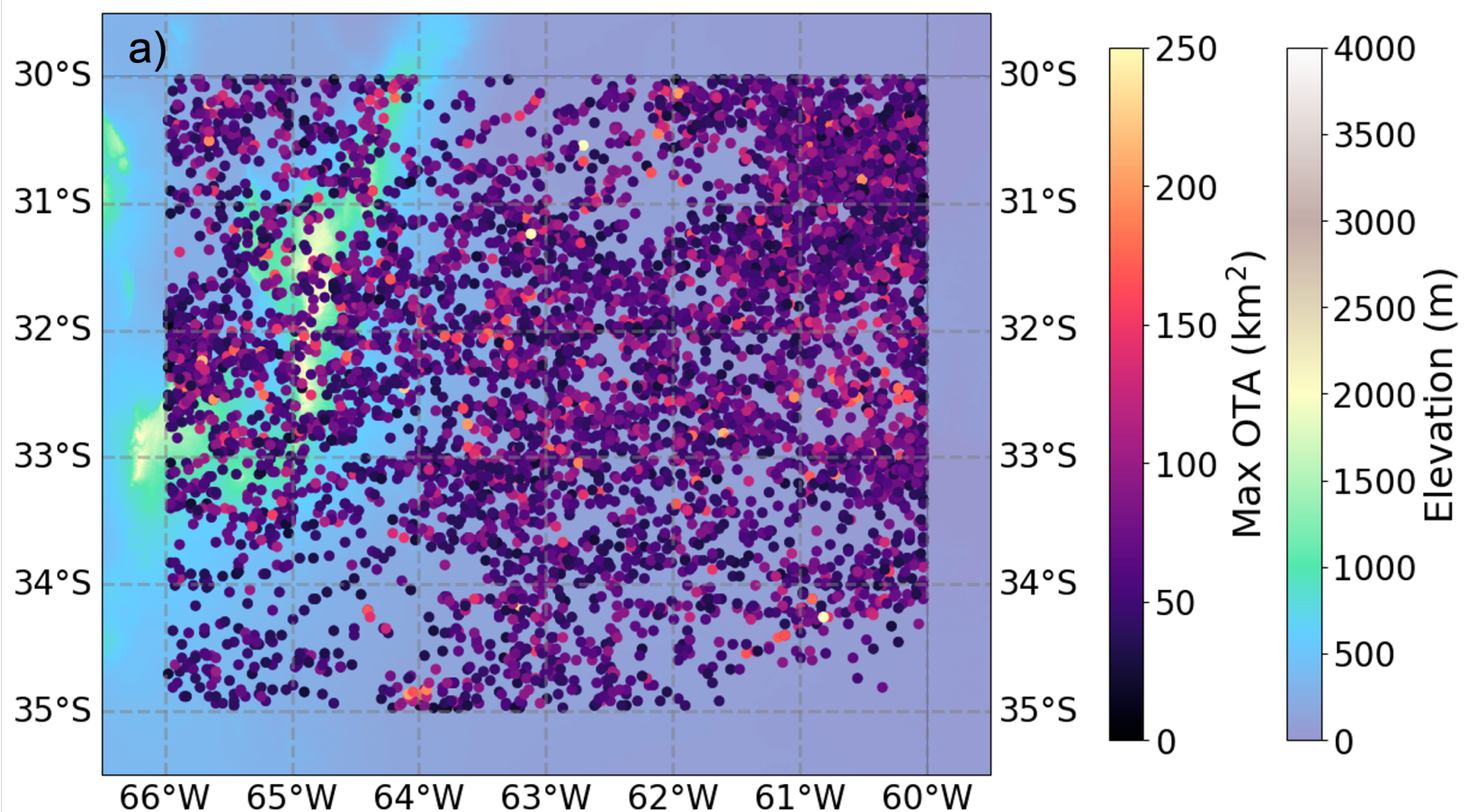
Observed $\bar{\Gamma}$ vs MERRA-2 $\bar{\Gamma}$, N = 50Observed $\overline{N^2}$ vs MERRA-2 $\overline{N^2}$, N = 50

Figure 5.

Max OTA, N = 5928

66°W 65°W 64°W 63°W 62°W 61°W 60°W



Max OTD, N = 5928

66°W 65°W 64°W 63°W 62°W 61°W 60°W

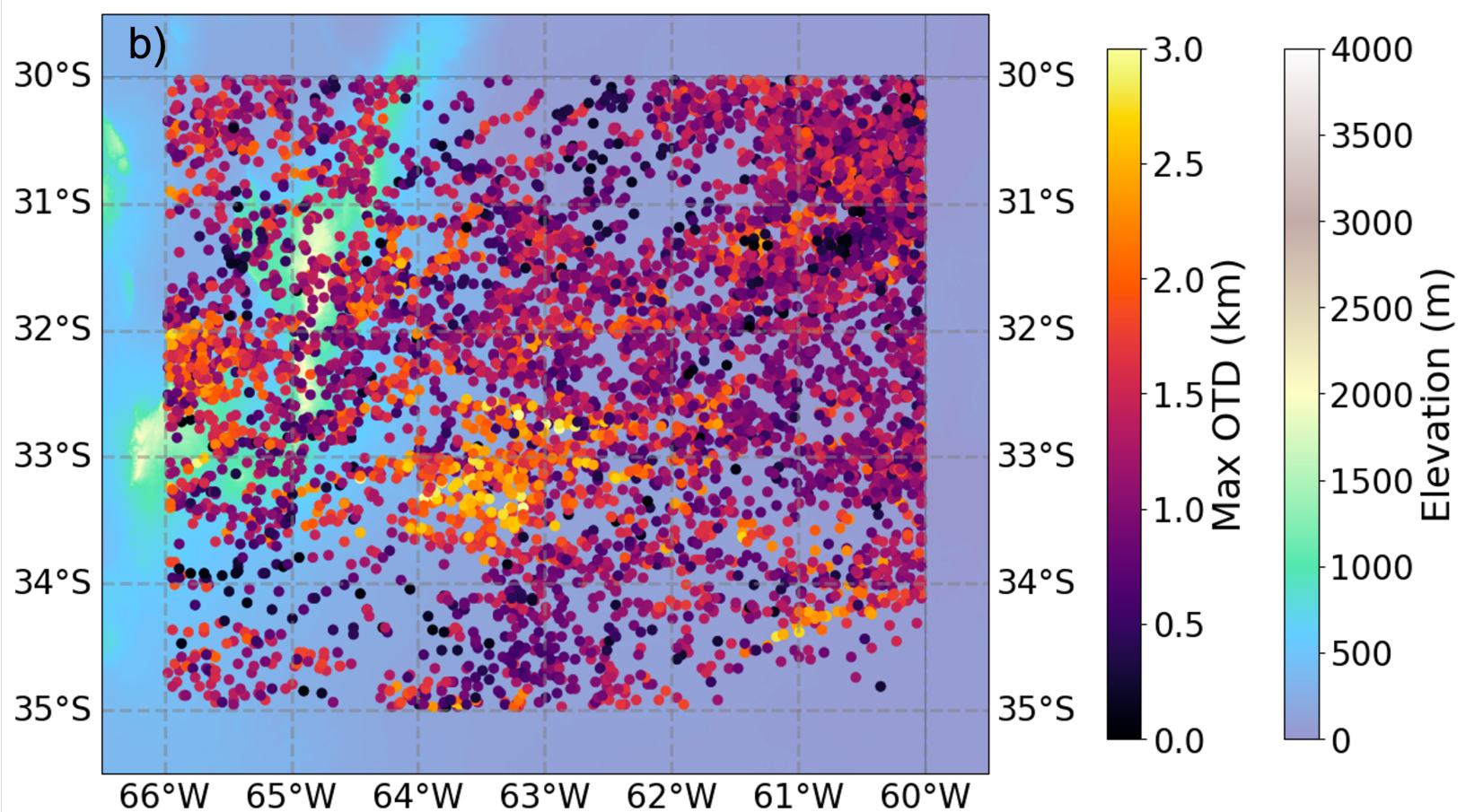


Figure 6.

Normalized Number of OTs per Hour, N = 28168

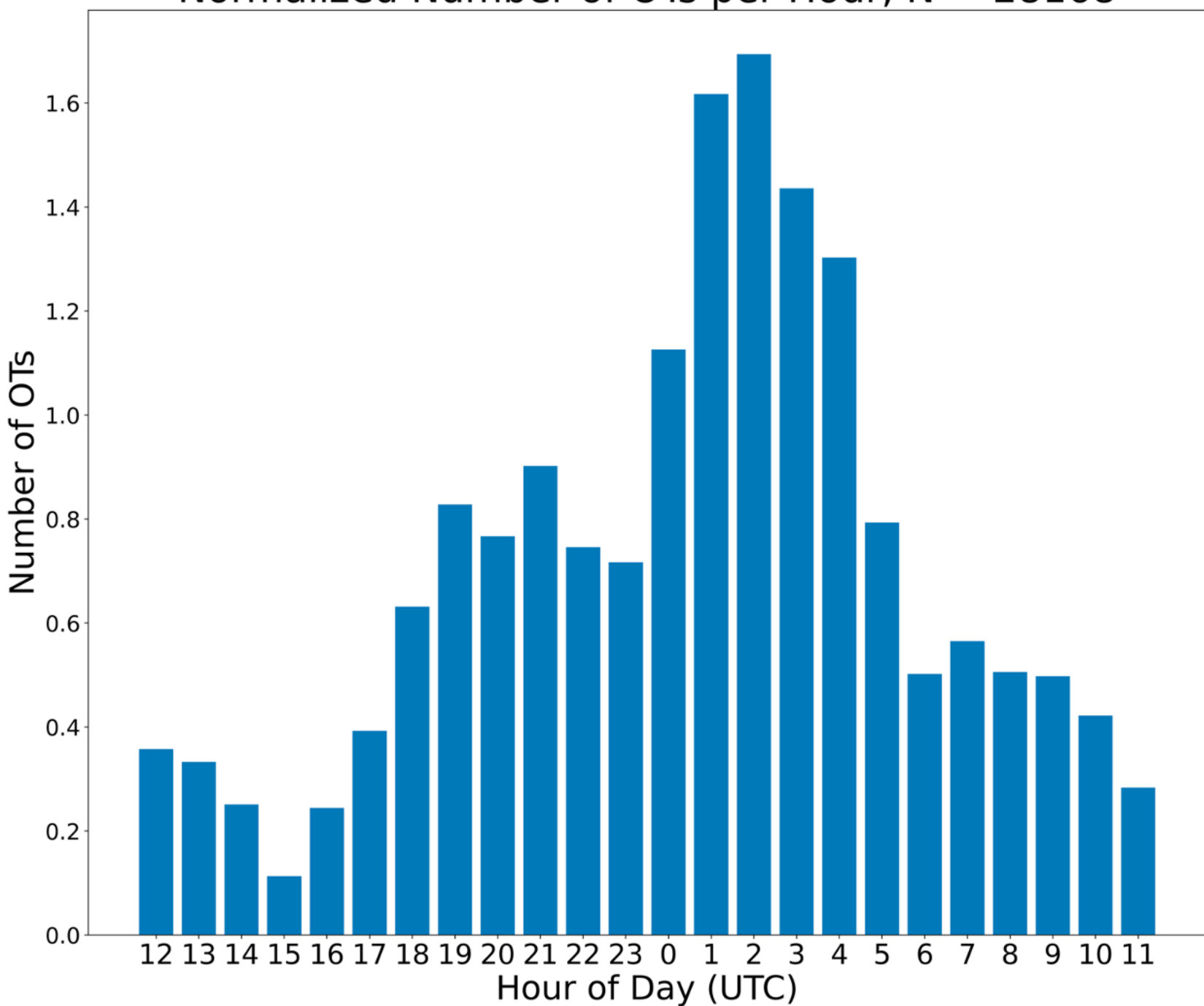
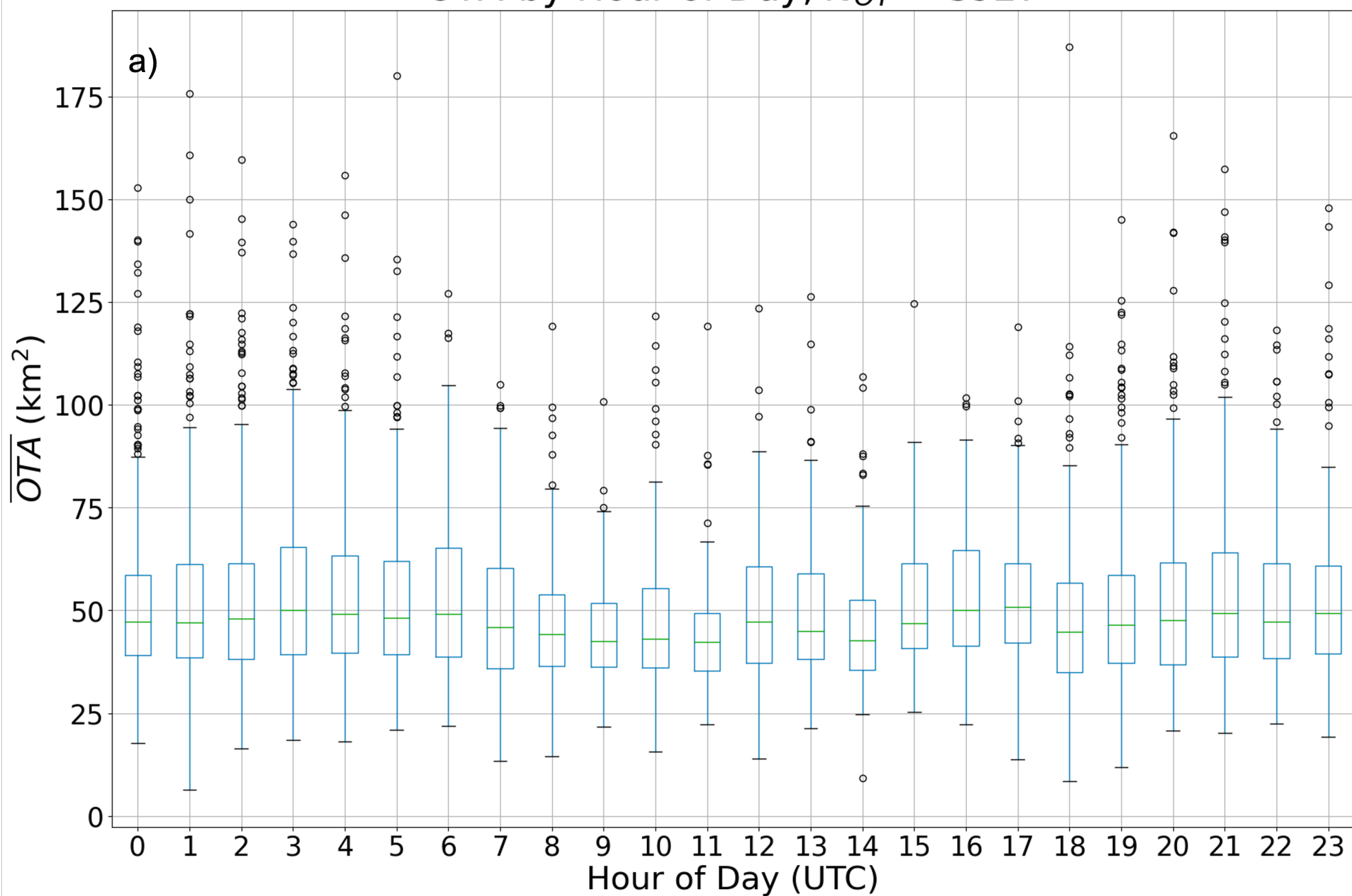


Figure 7.

\overline{OTA} by Hour of Day, $N_{OT} = 5927$



\overline{OTD} by Hour of Day, $N_{OT} = 5927$

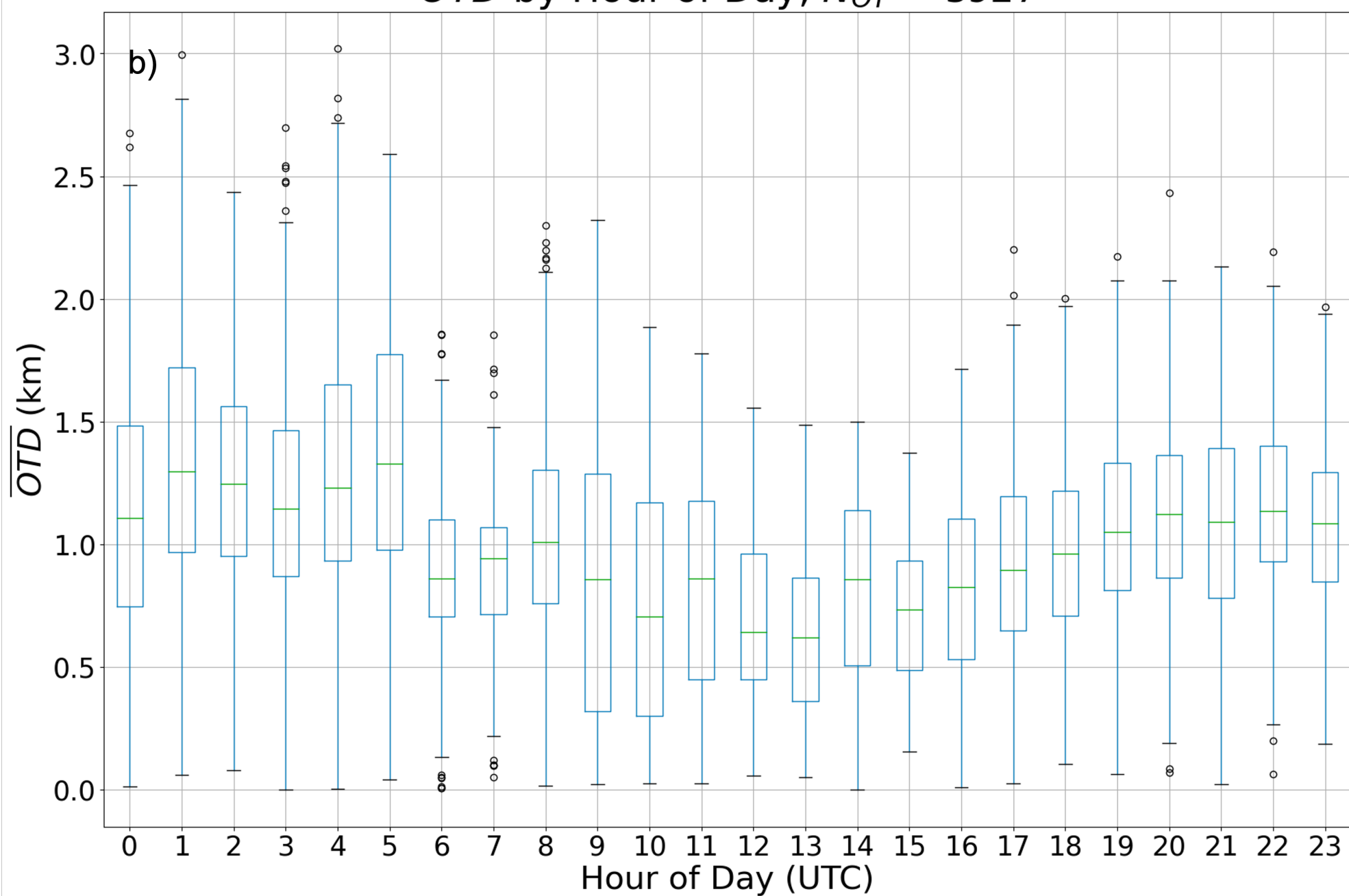


Figure 8.

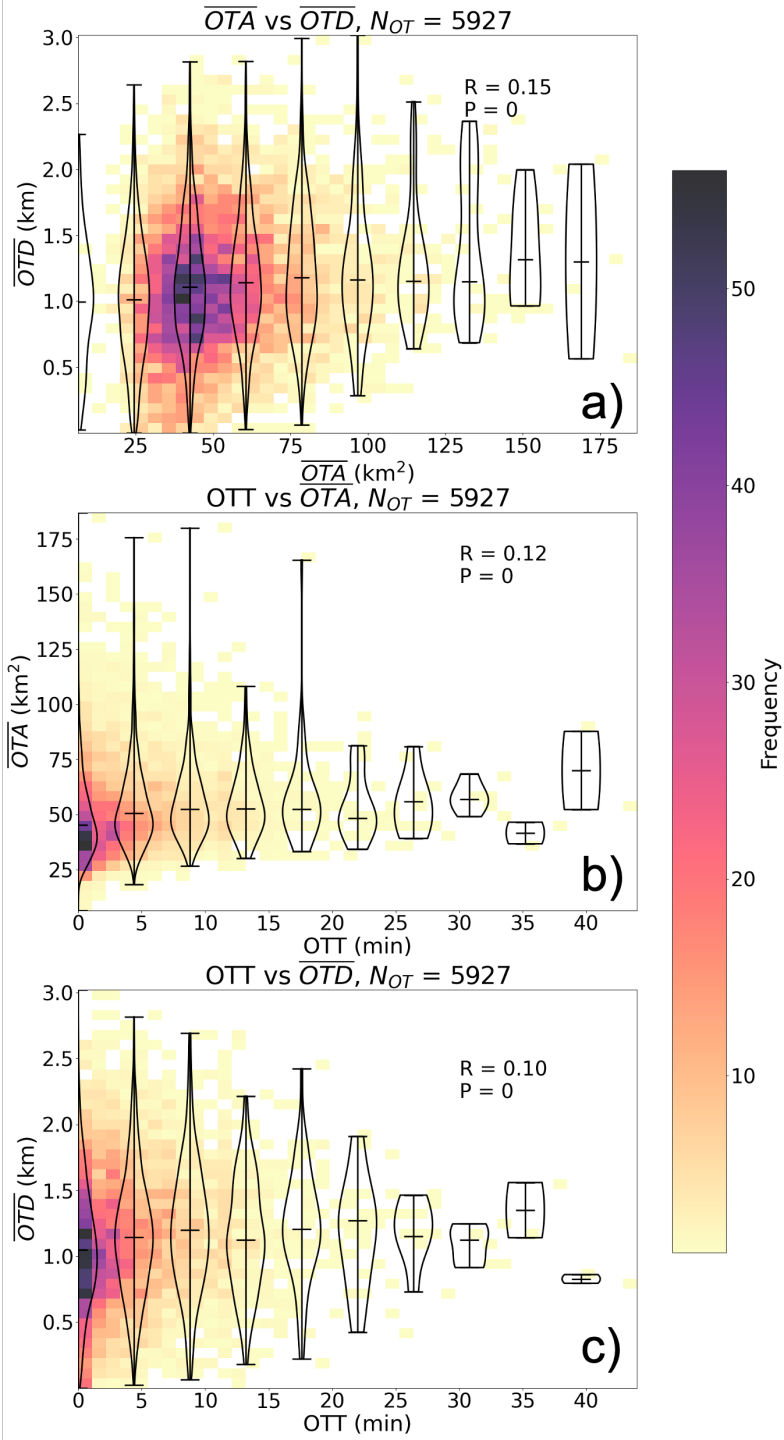


Figure 9.

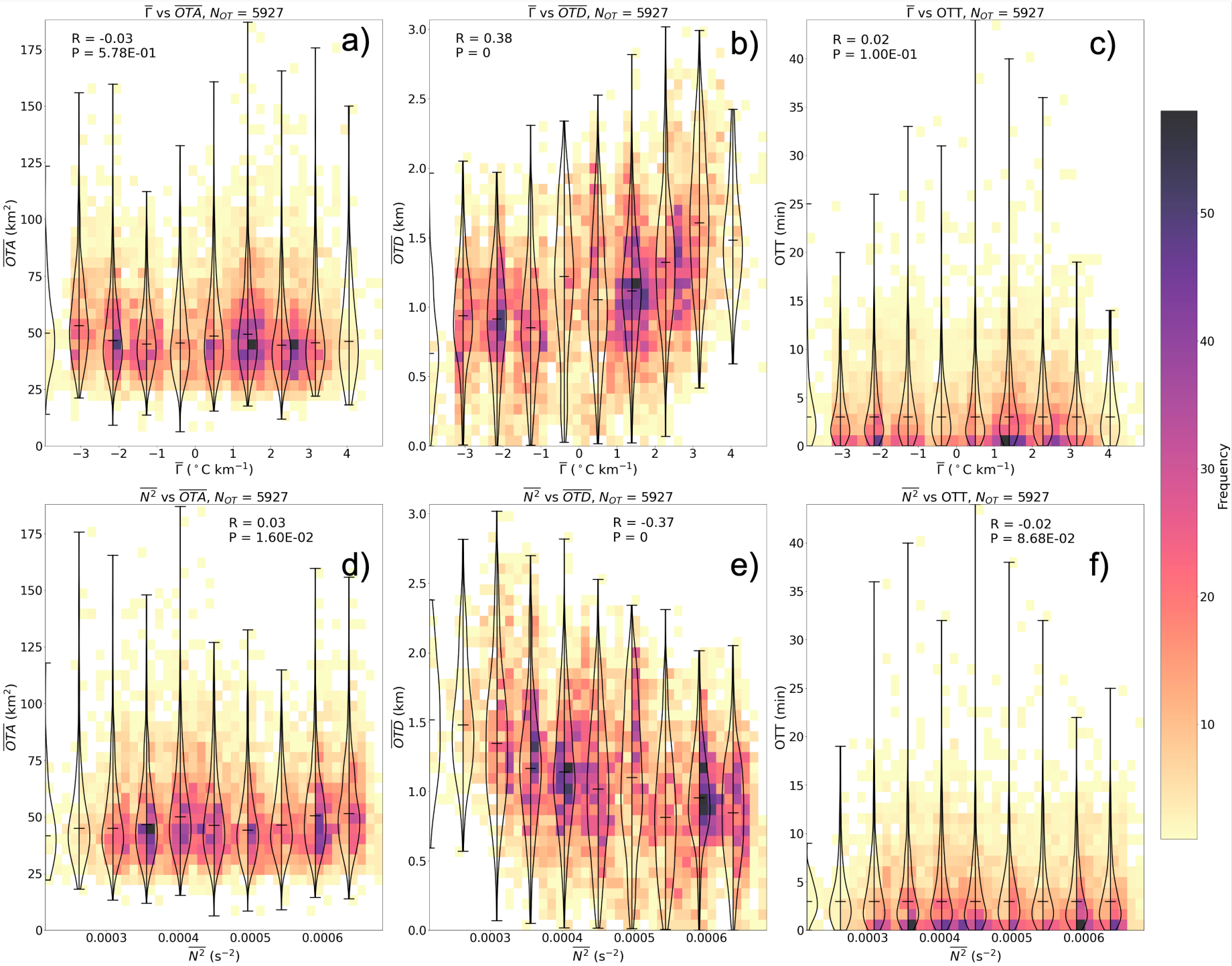
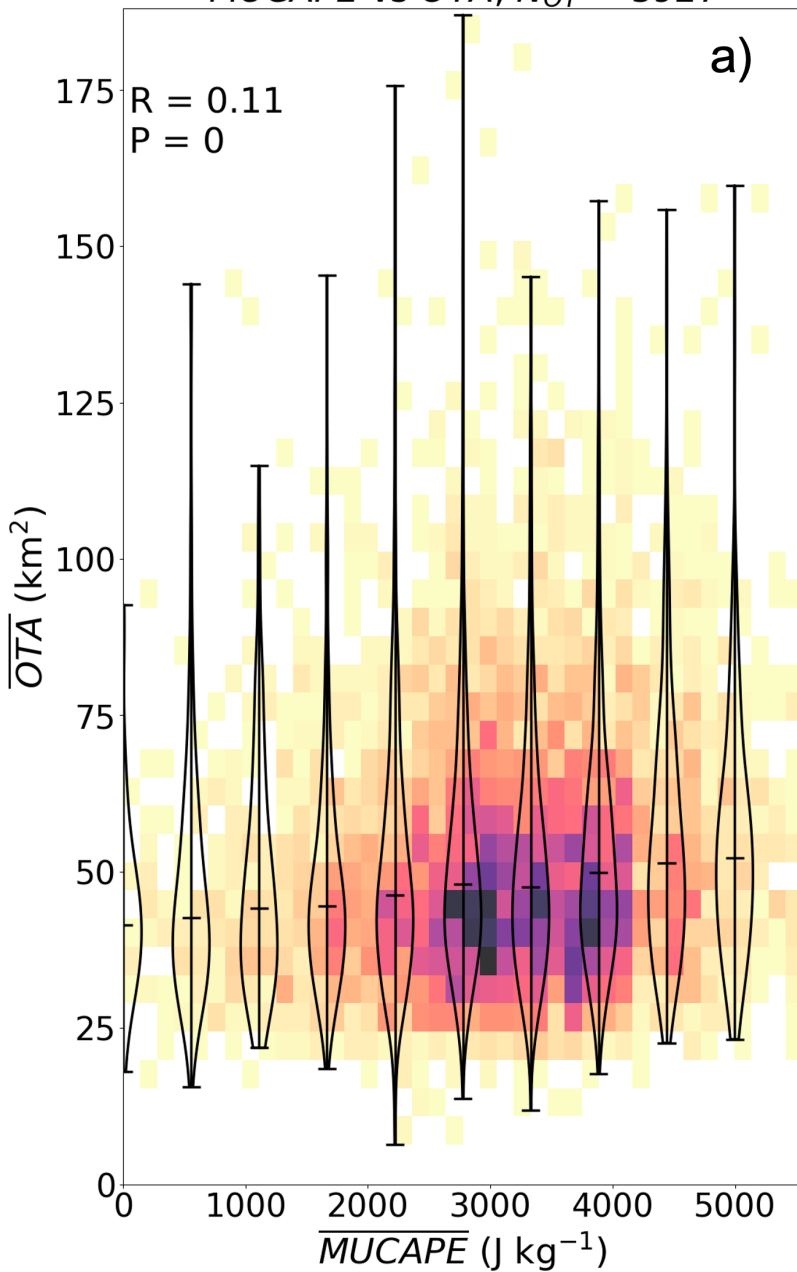
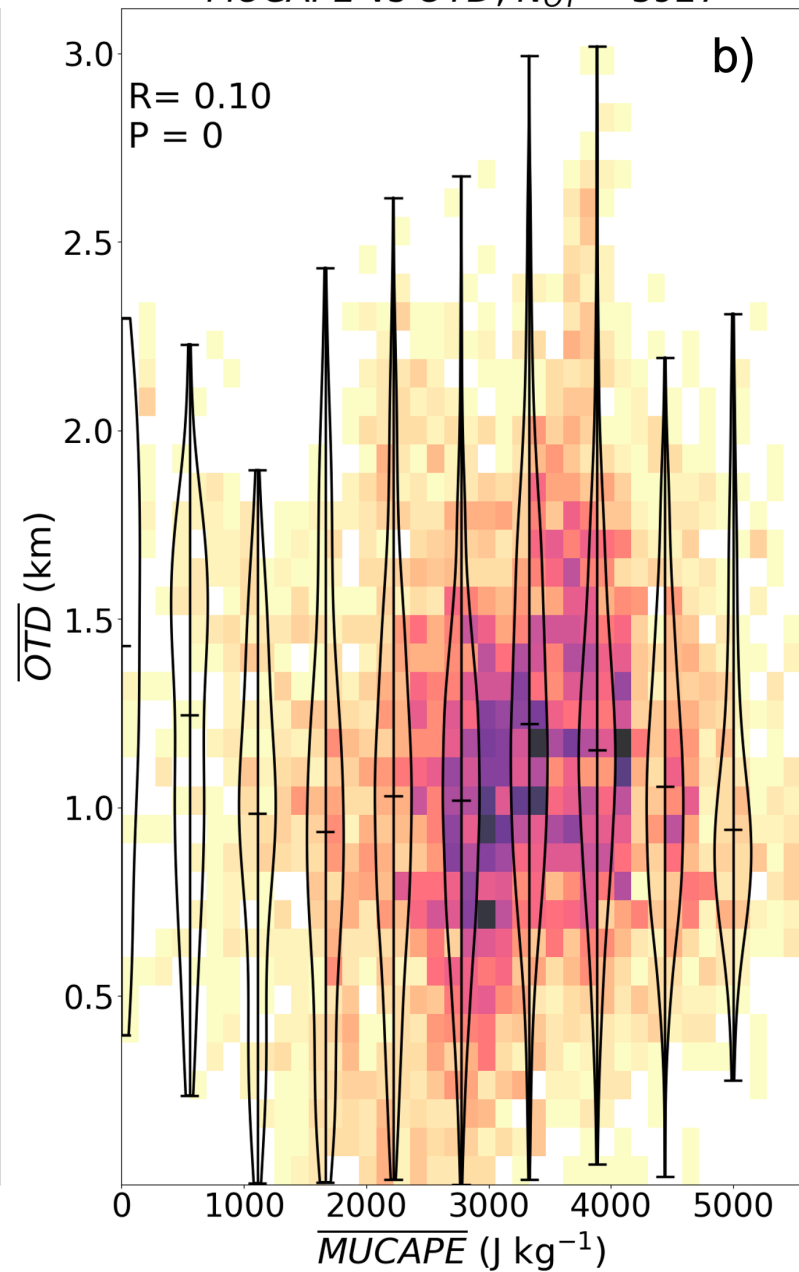


Figure 10.

\overline{MUCAPE} vs \overline{OTA} , $N_{OT} = 5927$



\overline{MUCAPE} vs \overline{OTD} , $N_{OT} = 5927$



\overline{MUCAPE} vs \overline{OTT} , $N_{OT} = 5927$

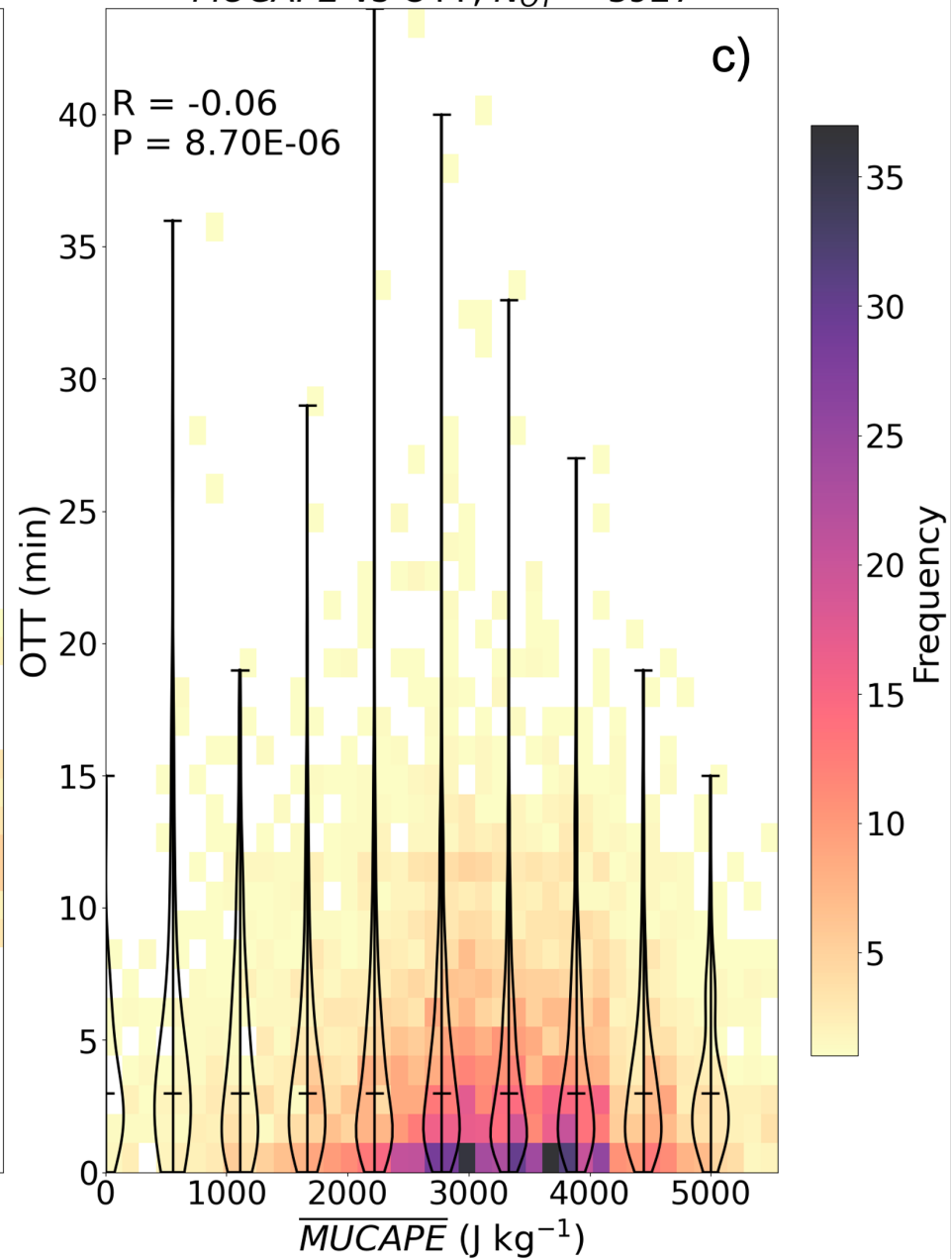


Figure 11.

